Heat transfer characteristics of heat exchanger elements in acoustic standing waves

By:

Shahin Amiri

Doctor of Philosophy

Department of Mechanical Engineering

McGill University

Montreal, Quebec

April 2014

A dissertation submitted to McGill University in partial fulfillment of the requirements for the degree of Doctor of Philosophy

Dedicated to

The best parents in the world, my parents.

Acknowledgements

I would like to express my sincere gratitude and appreciation to my supervisor, Professor Luc G. Mongeau, for providing me the opportunity to pursue this project. His expert knowledge in acoustics, fluid mechanics and heat transfer has guided my thesis to its completion. I deeply appreciate the support, freedom and understanding given to me.

I am thankful to Dr. Rani Taher for sharing his experience and for the support extended to me at the beginning when I started the project. I would also like to thank Dr. Yasser Rafat for his help and useful discussions during the experiments.

This work was supported by NSERC through a Discovery Grant, the Canada Research Chair program, and the Canadian Foundation for Innovations.

It was a great pleasure to work with my colleagues in the Acoustics Laboratory at McGill University. I am thankful for providing me such a friendly environment.

ABSTRACT

Thermoacoustic refrigerators use sound waves and the associated interactions between oscillatory gas particles and solid structures to transfer heat and generate cooling power. Heat exchangers are used to move the extracted heat from the periodic oscillatory flows. Heat transfer predictions based on steady state correlations are inaccurate for heat exchangers immersed in oscillating flows. The effects of flow oscillation on heat transfer characteristics related to vortex formation are not fully understood. The objective of the present study was to synchronously measure the flow velocity and the temperature fields and characterize the heat transfer from simplified heat exchanger geometries immersed in oscillatory flows typical of thermoacoustic systems.

Thermal and flow fields in the near field of three simplified heat exchanger geometries were visualized utilizing a synchronized PIV and PLIF technique. These configurations were investigated: 1) single cylinder, 2) tandem cylinders, and 3) finned tube. For the single cylinder case, cylinders with two different diameters were investigated independently. The results confirmed the reproducibility of the experimental data. For the tandem cylinders case, two different center-to-center distance to diameter ratios were chosen to investigate the effects of cylinder spacing and hydrodynamic interference. For the finned tube study, two longitudinal fins were attached to either side of a cylinder in order to better mimic the conditions of a real heat exchanger. The present work was the first systematic study to characterize heat transfer from simplified heat exchanger geometries subjected to oscillatory flow. Post processing of the visualization images allowed the determination of local time-dependent, spatially-averaged, and total heat transfer rates as a function of acoustic Reynolds number, Keulegan-Carpenter

number and dimensionless frequency parameter. The intermittent, time-varying vortex shedding behaviour of the flow caused a strong time dependence and a naturally unsteady heat transfer character. It was found that the vortex generation mechanism and heat transfer rates from bluff bodies immersed in oscillatory flows are totally different from those in steady state flows.

RÉSUMÉ

Les Réfrigérateurs thermo-acoustiques emploient les ondes sonores, l'interaction des particules de gaz oscillatoires et des structures solides de transfert de chaleur pour produire de l'énergie de refroidissement. Les échangeurs de chaleur ont un rôle essentiel pour déplacer la chaleur extraite et doivent être pleinement caractérisé lorsqu'ils sont soumis à débits oscillatoires. Les prévisions de transfert de chaleur basées sur des corrélations au régime permanent sont imprécises pour les échangeurs de chaleur immergés dans des débits oscillants. L'effet de l'oscillation de l'écoulement sur les caractéristiques de transfert de chaleur en relation avec la formation de tourbillons n'est pas entièrement élucidé. L'objectif de cette étude est de visualiser simultanément l'écoulement et les champs thermiques ainsi que de caractériser expérimentalement le transfert de chaleur d'échangeur de chaleur à géométries simplifiées soumis aux écoulements oscillatoires. Les Champs thermiques et d'écoulement dans le champ proche de trois géométries simplifiées d'échangeurs de chaleur ont été visualisés en utilisant un PIV synchronisée et la technique PLIF. Ces géométries incluent : 1) un seul cylindre, 2) cylindres agencés en tandem et 3) la configuration du tube à ailettes.Pour le cas d'un seul cylindre, des cylindres de deux diamètres différents ont été examinés séparément et dont les résultats ont confirmé la reproductibilité des données expérimentales. Pour le cas des cylindres en tandem, deux distances différentes de centre-à-centre pour des ratios de diamètres ont été choisis pour étudier l'effet de l'espacement des cylindres et des interférences hydrodynamiques sur le transfert de chaleur en écoulement oscillatoire. Pour l'étude des tube à ailettes, deux ailettes longitudinales ont étaient attachées sur chaque côté d'un cylindre, afin de mieux émuler un échangeur de chaleur réel. Le présent travail a été la première étude systématique pour la caractérisation du transfert de chaleur à partir d'échangeur de chaleur à géométries simplifiées soumis à un écoulement oscillatoire. Le post-traitement des images de visualisation a permis la détermination des taux de transfert de chaleur locaux en fonction du temps, moyennée spatialement, ainsi le total de transfert de chaleur en fonction du nombre de Reynolds acoustique, du nombre Keulegan-Carpenter et du paramètre de fréquence sans dimension. Le comportement de l'écoulement intermittent, variable dans le temps, et générateur de vortexa provoqué un transfert de chaleur naturellement instable et à forte dépendance du temps. Il a été conclu que le mécanisme de génération de vortex et les taux de transfert de chaleur à partir de corps non profilés immergés dans des écoulements oscillatoires sont totalement différents de ceux des flux aux régimes stables permanents.

LIST OF CONTENTS

LIST OF TABLES

LIST OF FIGURES

LIST OF SYMBOLS

Symbols

A	Cross-sectional area of the bluff body [m^2]
A_{max}	Displacement amplitude of oscillating flow [m]
C	Dye concentration [g/l]
C_D	Drag coefficient
C_M	Inertia coefficient
d	Diameter of the seeding particles [m]
D	Diameter of the cylinder [m]
f	Frequency of flow oscillation [Hz]
F_D	Drag force [N]
F_I	Inertia force [N]
F_x	Dimensionless axial force
F_x^*	Axial force per cylinder unit length [N/m]
g	Gravitational acceleration [m/s^2]
h	Heat transfer coefficient [$W/m^{2o}K$]
H	Channel height [mm]
I	Intensity of fluorescence light [W/m^3]

I_0	Intensity of incident laser light [W/m^3]
k	Thermal conductivity [W/m^{o}K]
KC	Keulegan-Carpenter number [$U_{max}/(f \times D)$]
l	Cylinder spacing, center-to-center distance [m]
L	Channel length [mm]
m	Slope of the calibration curve
M	Parameter in Eq. (2.7)
Nu_θ	Local Nusselt number
Nu_{sp}	Spatially-averaged Nusselt number
Nu_{tot}	Total Nusselt number
Pr	Prandtl number
r	Radial coordinate
R	Radius of the cylinder [m]
Re_{ac}	Acoustic Reynolds number [$U_{max}D/\upsilon$]
St	Stanton number
Stk	Stokes number
t	Time [s]
T	Temperature [^{o}C]
u	Velocity of oscillating flow [m/s]
$\dot{u}$	Acceleration of oscillating flow [m/s^2]

u_x	Axial component of the free stream velocity [m/s]
U_{max}	Velocity amplitude of flow [m/s]
W	Channel width [mm]
V	Volume of the bluff body [m^3]
X	Parameter in Eq. (2.7)

Greek symbols

α	Thermal diffusivity [m^2/s]
α_v	Thermal expansion coefficient [1/K]
β	Frequency parameter [$f \times D^2/\upsilon$]
ε	Dye absorption coefficient
φ	Dye quantum efficiency
λ	Laser wave length [nm]
υ	Kinematic viscosity [m^2/s]
ρ	Density [kg/m^3]
τ_k	Kolmogorov time scale [s]
τ_p	Particle response time [s]
θ	Angle from stagnation point [degree]
ω	Oscillation angular frequency [rad/s]

Subscripts

∞	Ambient condition
f	Film condition
flu	Fluorescence
ij	Arbitrary point
m	Measured
p	Particle
ref	Reference
s	At the cylinder surface

Abbreviations

DSC	Developed semi circumference
fps	Frame per second
HWA	Hot wire anemometry
PIV	Particle image velocimetry
PLIF	Planar laser induced fluorescence
TR	Time resolved

Chapter 1

Introduction

1.1 Motivation

The study of oscillatory flows is motivated in part by the prospect of applications of cooling technologies, based on the thermoacoustic cooling cycle. Thermoacoustic cooling is a technology in which cooling energy is obtained from high amplitude sound waves. There are significant environmental and technical advantages in using thermoacoustic technology compared to other cooling technologies [1]. From an environmental point of view, thermoacoustic devices (refrigerators, engines) use only environmentally friendly gasses such as helium and argon, and do not require the use of Chlorofluorocarbons (CFC), which increases the greenhouse effect and ozone depletion. The production of CFCs has been banned by the Montreal Protocol since 1996 [2]. From a technical point of view, thermocoustic systems benefit from a relatively simple design, and minimal moving parts. But reliability and costs have been obstacles to their success in the workplace.

Thermal interactions between oscillatory compressible gas particles and the solid boundaries of stacks and heat exchangers can result in heat transfer. The heat transfer process has been up to now believed to be based on the so-called thermoacoustic cycle. Swift [1] comprehensively reviewed thermoacoustic phenomena and technologies. The analytical and theoretical foundations of thermoacoustic refrigerators were developed by Rott [3]. There are two types of thermoacoustic cooling systems, based on the phase between the oscillating pressure and velocity: 1) standing wave; and 2) travelling wave coolers. Standing wave coolers feature three critical components illustrated in Fig. 1.1: 1) acoustic energy source; 2) stack; and 3) hot and cold heat exchangers. The sound power produced by the driver is converted into high amplitude sound waves which cause cooling along the stack. Heat is pumped within the boundary layer. The role of the stack is to magnify the overall heat pumped from the pressure node to the pressure antinode by increasing the useful area within small channels. The channels serve to store heat from the gas particles during the first half of one oscillatory cycle, and redistribute it to neighbouring gas particles during the second half of the cycle through a process known as the “bucket brigade” effect. Only particles within around one thermal penetration depth effectively transfer heat. Net cooling power is transferred from the hot to the cold heat exchangers, placed at the stack’s extremities. Fin-tube heat exchangers are the most common types of heat exchangers used in thermoacoustic applications. The role of the heat exchangers is to provide a path to a secondary cooling loop. Water is commonly used as a liquid within the secondary loop. This loop delivers the produced cooling power to the load.

1.2 Literature review

The available literature on simplified heat exchanger geometries immersed in oscillatory flows may be divided into velocity and thermal field studies.

1.2.1 Flow velocity measurements

Most previous studies have focused on the physics of oscillatory flows and the understanding of the underlying fluid mechanic phenomena. For theoretical studies of oscillatory flow past bluff bodies, the oscillation is usually assumed to be purely sinusoidal. This simplifies the investigation of flow structures in the shear layer and wake regions.

Williamson and Roshko [4] investigated the flow patterns around an oscillating single cylinder for Reynolds number within the range $300 < Re < 1000$. The Reynolds number is defined as

$Re = U \times D/v$ in which U is the free stream velocity, D is the cylinder diameter, and v is the kinematic viscosity of the fluid. They identified a number of vortex shedding modes dependent on the displacement amplitude and frequency of the oscillation and created a map showing the vortex shedding modes in the amplitude-frequency plane. Obasaju et al. [5] visualized the vortex pattern and measured the force over a circular cylinder in planar oscillatory flow. The oscillating flow was generated by utilizing the resonance of a U-tube water tunnel with a fixed cylinder immersed in the test section. The U-tube has been fully described by Singh [6]. The existence of four different flow regimes was observed depending on the amplitude and oscillation frequency of the oscillating flow. A very similar work to study the velocity field around circular cylinders in oscillatory flows was performed by Justesen [7].

John and Gharib [8] performed studies for a circular cylinder oscillation in both the streamwise and transverse directions for Reynolds numbers within the range $630 < Re < 950$. They observed qualitative changes in the wake structure due to the addition of the transverse oscillation to the streamwise oscillation, which in turn changed the lift force on the cylinder. Barrero-Gil [9] measured indirectly the in-line force coefficients on oscillating bluff cylinders (circular and square) in quiescent fluid at low Reynolds and Stokes numbers. The experimental approach consisted of free-decay tests of a spring-mounted cylinder submerged in a water tank. Huelsz and Lopez-Alquicira [10] reported an experimental technique to measure the acoustic particle velocity using a single hot-wire anemometer (HWA). This technique allows the determination of the velocity amplitude and phase in standing waves. The advantage of using HWA is that this method does not require seeding. But HWA does not allow the study of the flow field in tight spaces. The hot wire probe must be traversed for surveys of the velocity profile, which is not always practical.

Kang and Chen [11] investigated the lift forces and the motions of vortices around a circular cylinder in sinusoidal oscillatory flow using PIV for a Reynolds number range within 2500 < *Re* < 10000. Particle Image Velocimetry (PIV) is an optical method to measure the velocity and the direction of the flow based on the motion of seeded particles. The main advantage of PIV is that it provides two- or three-dimensional vector fields, while the other techniques yield the velocity at one single location. Hann and Greated [12, 13] described a method which allows measurement of the flow velocity and acoustic particle velocity instantaneously over an area using PIV techniques.

Nabavi et al. [14] performed measurements of acoustic and streaming velocities using PIV. The acoustic velocity fields were obtained by cross-correlation between two consecutive PIV images, whereas the streaming velocity fields were obtained by cross-correlation of consecutive PIV images at the same phase.

The flow around two circular cylinders in tandem arrangement is less understood in comparison to the flow around a single circular cylinder. For tandem cylinders, the flow around each cylinder is modified due to the presence of the other cylinder. This leads to a complex interaction between the vortices and the shear layers. Mahir and Rockwell [15] investigated the wake pattern and velocity spectra for a pair of cylinders in a tandem arrangement subjected to forced oscillations at *Re*=160. They used wake spectral measurement technique and visualized the flow field using hydrogen-bubble methods to investigate the effects of amplitude, frequency and cylinder spacing. It was observed that for the tandem cylinders configuration with a large center-to-center distance, *l/D*=5, the excitation frequency at which the near-wake structure locked into the motion of the cylinders is approximately the same as that for a single cylinder. Brika and Laneville [16] studied the flow interaction between a stationary upstream cylinder and a lightly damped flexible downstream cylinder with longitudinal spacing *l/D*=7-25 in tandem and staggered arrangements. The existence of two wake patterns around the resonance velocity was observed for the tandem cylinders arrangement.

Blanc-benon et al. [17] used PIV to study the flow field within the internal structure of a model thermoacoustic system. They investigated vortex formation near the edges of the thin and thick stack plates in a quarter-wavelength thermoacoustic cooling system. They found that the flow field around the edge of the thin stack plates exhibits elongated vorticity layers, while it is dominated by the shedding and impingement of the concentrated vortices for the thick stack plates.

Mao et al. [18] investigated the flow structures around the end of the stack of parallel plates in the oscillatory flow generated by an acoustic standing wave using PIV. The flow structure was found to be symmetrical and an attached pairs of vortices was observed for relatively small drive ratios, defined as the ratio of acoustic pressure amplitude and the mean pressure. When the drive ratios were increased, other flow patterns were identified which led to alternate types of vortex shedding. A similar study was performed by Berson et al. [19] to characterize the flow field at the end of the stack plates of a thermoacoustic refrigerator. Using PIV, the acoustic particle velocity was measured within the oscillating boundary layers on the stack plate. The results showed the generation of symmetric pairs of counter-rotating vortices at the termination of the stack plates at low acoustic pressure levels. Detachment of the vortices and symmetry break up was observed at higher acoustic pressure levels.

Jaworski et al. [20] focused their investigation on the entrance flow into the channels formed by a stack of parallel plates, placed in an acoustic resonator with oscillatory flow motion. PIV was used to investigate the flow structures in the entrance region. Following to the introduction of cross-sectional discontinuities, they observed a vortex formation and shedding during the fluid ejection and development of an entrance flow during the suction phase.

1.2.2 Temperature measurements

Heat transfer from reciprocating periodic flows over bluff bodies has applications such as thermoacoustic heat exchangers and for hot wire anemometers. The flow structure when the outer mean flow is periodically reversed, caused recirculated flows that impact heat transfer. The most common instrument to measure temperature is the thermocouple. Thermocouples have a relatively long response time, and thus yield time-averaged results. They can be inserted into the internal structures of thermoacoustic systems. Leong and Jin [21] produced an oscillatory flow using a piston-cylinder arrangement. They investigated the oscillating flow through a channel filled with aluminium foam subjected to a constant wall heat flux. They analysed the effect of the dimensionless displacement amplitude and oscillation frequency on the heat transfer and found that heat transfer in oscillating flows increases with the dimensionless displacement amplitude of the flow through a porous channel.

Mozurkewich [22] measured heat transfer from heated wires located at a velocity antinode in a standing acoustic wave. A transient method was used, in which the rate of heat transfer was deduced from the rate of change of temperature after heating was turned off. At very high displacement amplitudes, the Nusselt number was observed to follow a well-known steady flow, a forced convection correlation.

Gopinath and Harder [23] inserted thermocouples inside a cylinder and measured the convective heat transfer rates in an acoustic flow. They assumed that the cylinder was representative of a heat exchanger tube. They examined only the low-amplitude cases in which the particle displacement amplitude in the oscillatory flow is small, i.e. on the scale of the cylinder diameter. Two distinct flow regimes were identified in Gopinath and Harder’s study. The first regime was a laminar attached flow regime which showed the square root dependence of the Nusselt number on the Reynolds number. The second regime was an unstable regime in which vortex shedding was prevalent, contributing to higher heat transfer rates.

Mozurkewich [24] investigated heat transfer from transverse tubes adjacent to a thermoacoustic stack. Three simple heat-exchanger configurations were examined. Two configurations consisted of bare, parallel, water-carrying tubes oriented transverse to the mean acoustic flow. A third configuration consisted of a single layer of woven copper screen soldered to transverse tubes. Large heat transfer with a zero temperature difference between the heat exchanger and the stack was observed. Qualitatively, such heat flow occurred because the gas interacting with the heat exchanger did not have the same time-averaged temperature as the end of the stack.

Paek et al. [25] investigated the thermal performance of heat exchangers in a thermoacoustic cooling system. They also used thermocouples to measure the temperature and reported heat exchanger performance in terms of the Colburn-j factor, a non-dimensional heat transfer parameter. Paek et al. [25] attempted to model the behaviour of heat exchangers in oscillatory flows using steady flow correlations. Models based on the time-average steady flow equivalent (TASFE) approximation, the rms Reynolds number, and boundary layer conduction were investigated. A very similar study by Nsofor et al. [26] has showed that the use of steady flow correlations for the analysis of oscillatory flows could lead to significant errors.

Iwai et al. [27] measured the time- and space-averaged heat transfer coefficients of a circular cylinder immersed in a slowly oscillating flow with zero-mean velocity by using transient methods. The flow oscillation amplitude and frequency were changed in the range where the flow remained laminar and fluid particle displacement amplitude was 10 to 38 times larger than the cylinder diameter. Unique heat transfer characteristics were observed at the phases when the cross-sectional mean velocity was small or increasing from a small value. During such period, heat transfer was enhanced due to the local fluid motion induced by the vortices around the cylinder.

An attractive method to capture the temperature field within heated flow regions is the Planar Laser Induced Fluorescence (PLIF) technique, a minimally intrusive method based on available

PIV. Shi et al. [28] performed two-dimensional velocity and temperature field measurements using PIV and acetone-based PLIF, respectively. They placed a pair of mock-up heat exchangers side by side in a quarter-wavelength standing wave resonator in order to mimic the environment of a thermoacoustic system. The impact of thermal, inertial and viscous effects on the time-dependent velocity distributions was investigated. An overshoot in velocity and temperature distributions was identified. The overshoot in the velocity distribution was due to the viscous and inertial effects in the gas, while the overshoot in temperature distribution was due to the velocity overshoot and the combined effect of the viscous and thermal boundary layers. The heat transfer coefficient and the Nusselt number were not calculated, most likely due to insufficient spatial resolution of the PLIF images.

1.3 Objectives

As described in the previous sections, an accurate characterization of heat exchangers in oscillatory flows is needed for improving the overall performance of thermoacoustic cooling systems. The overall objective of this research was to perform fluid flow and thermal field visualizations within different simplified heat exchanger geometries exposed to oscillatory flows. The proposed geometries are shown in full details in Chapter 2 of the present study and include: a) single cylinder; b) tandem cylinders; and c) a simplified finned tube configuration.

A secondary objective was to quantify and characterize heat transfer in oscillatory flow based on geometrical and flow parameters such as oscillatory frequency and velocity amplitude. Very few studies of the coupled fluid flow and heat transfer from bluff bodies in oscillatory flows have been reported in the literature. To our knowledge, the effects of flow oscillation on the heat transfer characteristics related to vortex formation have not attracted much attention.

In the present study of bluff bodies exposed to oscillatory flow, Particle Image Velocimetry (PIV) was used to image the flow field and Planar Laser Induced Fluorescence (PLIF) to concurrently capture the thermal field. These optical methods can be minimally intrusive and they can provide detailed two-dimensional maps of the velocity and the temperature fields.

The simultaneous capture of the time-dependent velocity and temperature fields is useful to characterize the instantaneous heat transfer. Heat transfer predictions based on steady flow correlations are often used, but were found to be inaccurate [26]. There is a need for a better understanding of the thermal and fluid interactions between oscillatory gas particles and the solid structures, and the influence of vortex-shedding on the unsteady heat transfer from bluff bodies such as circular cylinder, tandem cylinders and finned tube configurations. This could lead to the development of more efficient environmentally friendly thermoacoustic cooling systems that can be substituted for conventional vapor compression coolers in certain niche applications.

1.4 Outline of the thesis

Chapter 1 of this thesis provides a literature review along with the motivation and objectives of the research. In Chapter 2, the necessary background and a description of the test section and experimental methods (PIV and PLIF) employed throughout this research is described. Chapter 3 discusses the accuracy of the experimental data and provides flow and thermal fields visualization around a single circular cylinder immersed in an acoustic oscillatory flow. The characterization of the heat transfer coefficient around two arrangements of tandem cylinders in oscillating flow is described in Chapter 4.

Chapter 5 provides the characterization of heat transfer from a longitudinal finned tube based on oscillatory frequency and velocity amplitude. Finally, the conclusion of the research, contribution and the general recommendations for the future works are provided in Chapter 6.

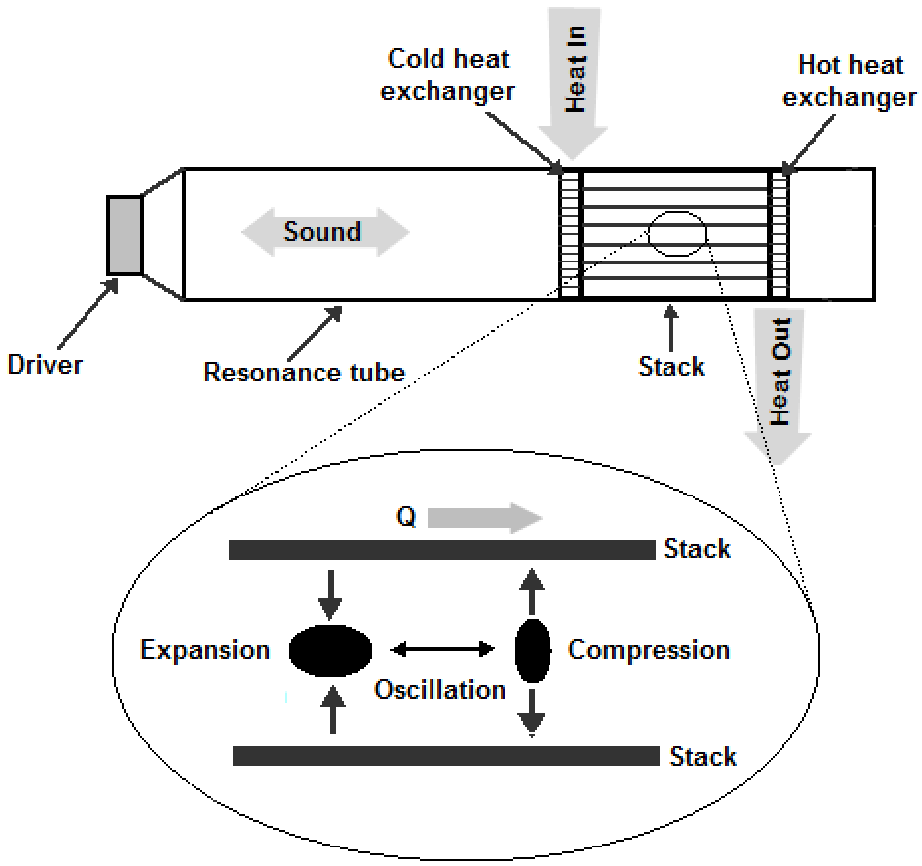

Figure 1.1. Schematic of a standing wave thermoacoustic refrigerator.

Chapter 2

Experimental apparatus and methodology

The experiments were performed in the Acoustics Laboratory, within the Mechanical Engineering Department at McGill University. Particle Image Velocimetry and Planar Laser Induced Fluorescence were employed to simultaneously capture the synchronous, time-dependent velocity and temperature fields around simplified heat exchanger geometries. A detailed description of the experimental apparatus and methodology is provided in this chapter.

2.1 Experimental apparatus

The experimental apparatus consisted of a water channel providing a zero-mean velocity oscillating flow. The three bluff body geometries investigated included a) one single cylinder; b) parallel tandem cylinder configurations; and c) one finned tube configuration.

2.1.1 Water channel

Experiments were conducted in a closed-cycle channel filled with deionised water. The channel dimensions were $L \times W \times H = 200 \times 40 \times 40$ mm, where L, W and H are the length, width and height, respectively. The channel walls were made of 5 mm thick Plexiglass. A schematic diagram of the water channel consisting a circular cylinder is shown in Fig. 2.1. The channel was installed on a horizontal vibration isolation table to minimize the influence of external perturbations. A T-type thermocouple was inserted into the channel to measure the water temperature. A 1 mm thick elastic silicon rubber membrane was located at each end of the channel. These membranes provided the required oscillatory motion through a cylinder piston connection. The blockage ratio is the ratio between the cylinder diameter and the channel height. The blockage ratio was lower than $D/H = 0.1$, where D is the cylinder diameter. This value is sufficiently low according to Cantwell and Coles [29] and Okajima et al. [30], and small enough to neglect the effect of channel walls. The entire experimental setup was located inside a room maintained at a constant temperature around 22 °C.

2.1.2 Cylinder and finned tube design

Stainless steel cylinders of two different diameters were used in this study. The outer diameter of the first cylinder was D=1.6 mm and the second cylinder outer diameter was D=4 mm. The use of different size cylinders allowed the reproducibility of the experiments to be investigated as discussed in chapter 3. Schematic diagrams of the single cylinder, tandem cylinders and finned tube configurations are shown in Fig. 2.2, with corresponding dimensions summarized in Table 2.1. The finned tube was made of copper and was built using Electrical Discharge Machining (EDM). The thermal properties of the cylinder materials at 25 °C are listed in Table 2.2.

A hole was drilled through the center axis of each cylinder and a very thin Ni-Cr resistance wire was inserted. This hole was filled with magnesium oxide powder to increase the thermal conductivity between the tube and the heater wire. Heat was provided by a DC power supply (BK Precision Model 1697) through the resistance wire. A very thin T-type thermocouple was inserted into the center of the heated length along each cylinder axis to measure the cylinder temperature. The cylinder and tube orientation was vertical inside the water channel. Ceramic rings were attached to both ends of the cylinder in order to reduce heat transfer between the cylinder and the Plexiglass walls. The cylinder temperature was kept constant within the range between $22 < T_s < 40$ °C.

2.1.3 Actuation mechanism

Fig. 2.3 shows a schematic diagram of the test section. A sinusoidal oscillatory motion was imposed using an acoustic subwoofer (TC Sounds LMS-R 15 DVC) as a linear actuator. The vibrating core was attached to one of the silicon membranes through a cylindrical piston connection. The shaker was driven by an acoustic audio amplifier (100 W RMS into 4 Ohms). The sinusoidal signal was fed to the amplifier using a digital signal generator (InSTEK GFG-8216A).

The frequency and the amplitude of the zero-mean velocity oscillations varied depending on the diameter of the cylinders. With this system, it was possible to set the frequency of the oscillating flow within the range of $7 \leq f \leq 35$ Hz, and velocity amplitude, U_{max}, in the range between 0.09 to 1.32 m/s. The Buckingham π theorem was applied to describe all the results in terms of dimensionless parameters. This theorem takes into account all the independent variables (such as velocity, viscosity, cylinder diameter and oscillation frequency) and provides a shorter list of dimensionless parameters. By applying the Buckingham π theorem to the bluff bodies immersed in oscillatory flows, the acoustic Reynolds number and Keulegan-Carpenter number were obtained as the required dimensionless parameters. The acoustic Reynolds number is defined as $Re_{ac} = U_{max}D/\nu$, in which ν is the kinematic viscosity of the fluid. The acoustic Reynolds number varied between $451 < Re_{ac} < 7096$. The Keulegan–Carpenter number, defined as $KC = U_{max}/(f \times D)$, varied between $3.14 < KC < 15.71$. This nondimensional parameter describes the relative importance of the drag forces over inertia forces for bluff bodies immersed in an oscillatory fluid flow. Drag and inertia forces are defined as $F_D = \frac{1}{2}\rho C_D A u^2$ and $F_I = \rho C_M V \dot{u}$, respectively in which ρ is the density of the fluid, C_D is the drag coefficient, A is cross-sectional area of the bluff body perpendicular to the flow direction, u is the velocity of oscillating flow, C_M is the inertia coefficient, V is the volume of the bluff body, and $\dot{u}$ is the acceleration of the oscillating flow. The dimensionless frequency parameter is obtained by divining the acoustic Reynolds number over Keulegan-Carpenter number. The range for the frequency parameter, β, defined as $\beta = f \times D^2/\nu$ was $82 < \beta < 451.7$ depending on the cylinder diameter and oscillation frequency.

2.2 Particle Image Velocimetry (PIV)

Particle Image Velocimetry is an optical method to visualize and quantify two-dimensional or three-dimensional flow velocity fields. It is widely used in experimental fluid mechanics to acquire instantaneous full-field velocity vector maps [17-20]. The applications include vortex formation analysis, aerodynamics, jet impingement and combustion. This technique is minimally intrusive and causes a minimum distortion to the flow field if the material and the size of the seeding particles are chosen appropriately. The principles of Particle Image Velocimetry are described in the following sections.

2.2.1 Seeding particles, laser, and camera

Seeding particles were added to the water channel to follow the fluid flow. The choice of the proper seeding particles depends on the nature of the flow, fluid density and the light scattering properties. The particles should have the same density as the flow and should be small enough to be entrained without disturbance. For the present study, the deionised water channel was seeded with polymer microsphere particles (Thermo SCIENTIFIC #7508A). The average diameter of seeded particles were $d_p = 7.9$ µm with a specific weight of 1.05 g/cm^3. These particles were naturally buoyant in water and remained suspended as water oscillated through the channel. According to the suggestions of Marchioli et al. [31], the Stokes number was calculated to check the behaviour of particles suspended in the water channel. The Stokes number is the ratio of the particle response time to the Kolmogorov time scale as

$$Stk = \frac{\tau_p}{\tau_k} \quad , \tag{2.1}$$

and

$$\tau_p = \frac{\rho_p d_p^2}{18\,\mu} \quad , \tag{2.2}$$

where τ_p is the particle response time, τ_k is the Kolmogorov time scale, and ρ_p is the particle density. The Stokes number was found to be 0.12 at most, i.e. it was much less than unity. It was therefore assured that the presence of the particles had minimal influence over the flow field.

A sketch of the basic principles of PIV is shown in Fig. 2.4. The seeding particles are illuminated by a laser sheet. The pulsed illumination laser sheet was generated using a time-resolved double-pulsed Nd:YLF laser system (Litron LDY 302) with a wavelength of λ=532 nm and a maximum repetition rate of 10 kHz per cavity. This PIV system was able to provide both phase-locked and time-resolved data. The phase-locked mode is generally used to find the velocities of time-dependent steady flows or pulsatile flows at certain phases, while the time-resolved mode is able to capture the flow field evolution with a very high temporal resolution. Using a combination of spherical and cylindrical lenses, the laser beam was collimated in a planar laser sheet less than 1 mm thick. In order to align the laser sheet, the laser cavity was placed on two precision vertical jacks. The laser sheet was aligned such that it was perpendicular to the cylinder axis. The frequency of the double-pulsed illumination was 1000 Hz.

The light scattered by the seeding particles was recorded using a high temporal resolution CMOS camera, a NanoSense MKIII with 1280×1024 pixels resolution. The double-pulsed Nd:YLF laser and the recording camera were connected to a host computer via a synchronizer. The timing of the laser illumination and the image acquisition were controlled by the commercial software DynamicStudio.

2.2.2 Data processing

Calibration tests were performed to establish the effect of camera lens magnification, and determine the transfer function between the digitized image on the camera sensor and the actual image. The PIV images were recorded in double frame mode in which two images were captured each time one trigger signal activates the laser. The recorded frames were split into a large number of subareas called interrogation areas or windows. The time delay between two frames was determined based on the flow velocity such that the particle displacement between the two frames was approximately one quarter of the interrogation window. In order to improve the quality of the raw captured images, the minimum intensity of each ensemble of images was calculated and then subtracted from all the images of the ensemble. This procedure enhanced the signal to noise ratio by increasing the sharpness of the raw images.

Using post processing software, the displacement of each seeding particle between two successive light pulses was calculated. The displacement vector of each interrogation area was determined using cross correlation techniques. Then the velocity vector was calculated using the time between two successive light pulses and the physical size of each pixel on the recorded images. Keane and Adrian [32] showed that at least ten tracer particle images per interrogation window are required to accurately resolve local particle displacement using conventional correlation analysis based on image-processing algorithms. A total of 3000 successive frames (18.75 μm/pixel resolution and 16 by 16 pixel interrogation window size) were acquired at 1000 frames/s for each run, which produced 28 to 142 velocity frames per cycle, depending on the excitation frequency.

2.3 Planar Laser Induced Fluorescence (PLIF)

Planar Laser Induced Fluorescence is an optical diagnostic method to visualize two-dimensional flow field variables including, concentration, density and temperature. It is widely used where instantaneous full-field temperature maps are required such as in engines, furnaces and boilers. This technique is to a large degree non-intrusive and causes a minimal distortion to the flow field. The basics of PLIF and the hardware used during this study are described in the following sections. A graphical illustration of the basic idea behind PLIF is shown in Fig. 2.5.

In PLIF, fluorescence dyes (tracers) are added to the fluid of interest which is illuminated by a laser light sheet. The fluorescence molecules are excited by the laser sheet light. The ground state molecules of the fluorescence dyes absorb the incident laser light and then are excited to a higher electronic energy state. These excited molecules are then relaxed to a lower energy level and emit fluorescence light which can be captured on a digital camera. The recorded fluorescence signal is proportional to the population of the excited state. This population is itself dependent on the temperature of the fluorescence dyes, so a two-dimensional temperature field can be obtained.

2.3.1 Fluorescence dye, laser, and camera

Rhodamine B with a concentration of 10^{-5}g/l was used as the fluorescent dye for PLIF temperature measurements. The basic characteristics of Rhodamin B are summerized in Table 2.3. This dye is made of organic molecules with aromatic ring structures, which possess delocalized electrons that can be easily excited by photons. The fluorescent molecules were approximately 10 nm [33] and were soluble in water.

The same time-resolved double-pulsed Nd:YLF laser used for the PIV measurements provided the laser beam for the PLIF visualization. An image recording system was employed using a high speed CMOS camera, a Photron FASTCAM MC2 with 512×512 pixels resolution. A narrow-band red filter (570 nm cut-off wavelength) was installed ahead of the PLIF camera, so only the fluorescence light was recorded. A synchronizer connected the double-pulsed Nd:YLF laser and the recording camera to a host computer.

2.3.2 Data processing

Following Coppeta and Rogers [34], for a low concentration of dye (e.g., 10^{-5}g/l in this study), the intensity of the laser induced fluorescence light I (W.m^{-3}), at any arbitrary point (i, j) when illuminated with an incident laser light of intensity I_0 (W.m^{-3}), can be expressed as

$$I = I_0 C \phi \varepsilon\,, \tag{2.3}$$

where C is the dye concentration, ε is the absorption coefficient of the dye and φ is its quantum efficiency. In the case of Rhodamine B, variations in I with temperature are attributable to the temperature dependence of the quantum efficiency [35]. To obtain whole-field quantitative temperature distribution in the flow field, a calibration procedure was followed. Several reference field image sequences at uniform temperatures were obtained for a fixed optical setting. The linear relationship between the measured temperature, $T_{m,ij}$, in the objective fluid flow and the measured digital signal level, $I_{m,ij}$, can be expressed by the equation

$$T_{m,\,ij}=\frac{I_{flu,\,ij}}{m}+T_{ref}\,, \tag{2.4}$$

where m is a constant value and T_{ref} is the temperature at a reference condition. Furthermore

$$I_{flu,\,ij}=I_{m,\,ij}-I_{ref}\,, \tag{2.5}$$

where $I_{m,,ij}$ is the red-scale image intensity of sequences (21.5μm/pixel) obtained simultaneously with PIV image acquisition (1000 frames/s) and I_{ref} is the red-scale intensity obtained from averaged sequence images (100 images are recorded) acquired at the uniform reference temperature.

Calibration experiments were done to determine the relation between the temperature and fluorescence intensity. According to the study performed by Coolen et al. [36], self-absorption can be neglected for low dye concentrations. The water temperature was increased by means of a heater over the temperature range between 22-40 °C. T-Type thermocouples were used to measure the water temperature inside the channel. The relation between fluorescence intensity and temperature is shown in Fig. 2.6. This relation was approximated by a linear least square fit. The accuracy of the temperature estimates was obtained as ±0.25°C, with a 97% confidence.

2.4 PIV and PLIF synchronization

Fig. 2.7 shows the test section and the synchronized PIV and PLIF cameras. Synchronous temperature and velocity measurement provides a full visualization map in which the effect of vortices motion on heat transfer can be studied in more detail. In this case, two high speed cameras recorded the PIV and PLIF images. A synchronizer (Dantec Dynamics 80N77) connected the PIV and PLIF recording cameras to a host computer. The timing of the laser illumination and the image acquisition were controlled by the commercial software DynamicStudio.

2.5 Determination of heat transfer coefficient

Each image of the temperature field was read by a MATLAB script. By selecting three arbitrary points on the cylinder perimeter, the radius and the center of the cylinder in X-Y coordinates were calculated as illustrated in Fig. 2.8. In order to calculate the temperature gradient on the heated surface, the intensity of each pixel was collected along radial and vertical lines, using MATLAB. The vertical lines were used to read the pixel intensity in the direction perpendicular to the fin surface. The radial lines with interval of 10 or 15 degrees were used to read the pixel intensity in the direction normal to the cylinder surface, as illustrated in Fig. 2.9. Then, an exponential curve fitting, $a+b\times e^{-r/c}$, was employed to fit the collected intensity data along the vertical and the radial lines. The coefficients a, b, and c were calculated using the method of least squares. This curve fitting provided the intensity gradient on the heated surface Fig. 2.10 shows the intensity distribution and the corresponding fitted curve along the radial direction "o-a" (30 degree) and vertical direction "b-c".

The temperature field and temperature gradient on the fin and cylinder surface were obtained using intensity-temperature calibration data. Finally, the local Nusselt number was calculated using the equation

$$Nu_\theta = \frac{h_\theta D}{k_f}, \tag{2.6}$$

where, k_f is the thermal conductivity of the fluid at the film temperature and h is the local heat transfer coefficient defined as

$$h_\theta = \frac{-k_s \frac{\delta T}{\delta r}]_{r=R}}{T_s - T_\infty}. \tag{2.7}$$

In Eq. 2.5, r is the radial direction normal to the cylinder surface, T_s is the cylinder surface temperature, T_∞ is the ambient temperature, and k_s is the thermal conductivity of the fluid at the surface temperature.

The total Nusselt number, Nu_{tot}, was obtained from the equation

$$Nu_{tot} = \frac{1}{t_2 - t_1} \int_{t_1}^{t_2} Nu_{sp}\, dt, \tag{2.8}$$

in which the time period between t_1 and t_2 covers twenty cycles of oscillation.

2.6 Uncertainty analysis

An uncertainty analysis was carried out using the method described by Moffat [37]. In this method, for a value of M, whose results depend on uncorrelated input estimates X_1, X_2, . . .X_N, the uncertainty of the measurement was obtained by appropriately combining the uncertainties of these input estimates. The standard uncertainty of the value R was calculated using

$$M = M(X_1, X_2, \ldots, X_N), \tag{2.9}$$

and

$$\delta M = \left\{ \sum_{i=1}^{N} \left(\frac{\partial M}{\partial X_i} \delta X_i \right)^2 \right\}^{1/2}. \tag{2.10}$$

The uncertainties related to the water Prandtl number, thermal conductivity and kinematic viscosity were neglected. The tolerance and uncertainty of the cylinder diameter was obtained from the standards of the electrical discharge machining. The uncertainty associated with the oscillatory velocity measurement was less than 1.75%. The uncertainties of the thermocouples and the frequency generator were 0.25 ^{o}C and 0.01 Hz, respectively. The error sources are tabulated in Table 2.4. Using above parameters and the method described by Moffat [37], the overall error in measuring the local Nusselt number was evaluated to be at most 8.6%.

2.7 Experimental procedures

Fig. 2.11 shows the components of the experimental set-up. The vertical circular cylinder inside the test section (i) was heated by a DC power supply (b) through the resistance wire. A power analyzer (c) was connected to the power supply to monitor the voltage, current and power fed to the heated cylinder. The sinusoidal oscillatory motion was imposed using an acoustic subwoofer (h). The vibrating core of the subwoofer was attached to one of the silicon membranes of the test section. The subwoofer was driven by a 100 W RMS acoustic audio amplifier. The sinusoidal signal was fed into the amplifier from a digital signal generator (a). The particle image velocimetry (PIV) system was a dual-cavity, time-resolved Nd:YLF laser (d). A high-resolution CMOS camera, NanoSense MKIII (e), with a frame rate of 1000 fps was used to capture PIV images. PLIF images were captured by a high-resolution Photron camera, FASTCAM MC2 (f) with the frame rate of 1000 fps. The images were recorded in a computer (g) for post processing process.

Some preliminary investigations were performed for each configuration to optimize the polymer particles and Rhodamine B concentrations and to locate the appropriate position of the PIV and PLIF cameras. Three different simplified heat exchanger configurations were chosen including: a) single circular cylinder; b) arrangement of tandem cylinders; and c) finned tube configuration. For each configuration, experiments were conducted by changing the oscillation frequency and the amplitude of the oscillating flow velocity. Based on the cylinder diameter and the oscillating velocity amplitude, the experimental results presented in this study correspond to acoustic Reynolds numbers in the range of $451 < Re_{ac} < 7096$.

Table 2.4. Cylinder and finned tube dimensions.

	Small diameter cylinder (Single cylinder test)	Large diameter cylinder (single cylinder and tandem cylinders test)	Finned tube
Outer diameter (mm)	1.6	4	4
Inner diameter (mm)	1.2	3	3
Length (mm)	40	40	40
Heated Length (mm)	35	35	35
Fin length			2
Fin thickness			1

Table 5.2. Cylinder material properties.

	Stainless steel 310	Copper
Density, ρ (kg/m^3)	7840	8960
Thermal conductivity, k (W/m.K)	16	401
Specific heat Capacity, C_p (J/kg.K)	490	390
Thermal diffusivity, α (m^2/s)	3.35×10^{-6}	1.11×10^{-4}

Table 2.3. Basic characteristics of Rhodamine B dye at T=20 ºC.

Dye	Molecular weight	$\lambda_{absorption}$ peak (nm)	$\lambda_{emission}$ peak (nm)
Rhodamine B	479.02	554	575

Table 2.4. Sources of experimental uncertainties.

	Variable	Uncertainty
Temperature	T	0.25 ºC
Cylinder diameter	D	0.02 mm
Frequency	f	0.01 Hz
Velocity	u	0.0175 mv*
Acoustic Reynolds number	Re_{ac}	0.03 mv
Keulegan-Carpenter number	KC	0.035 mv
Frequency parameter	β	0.03 mv

* Measured value

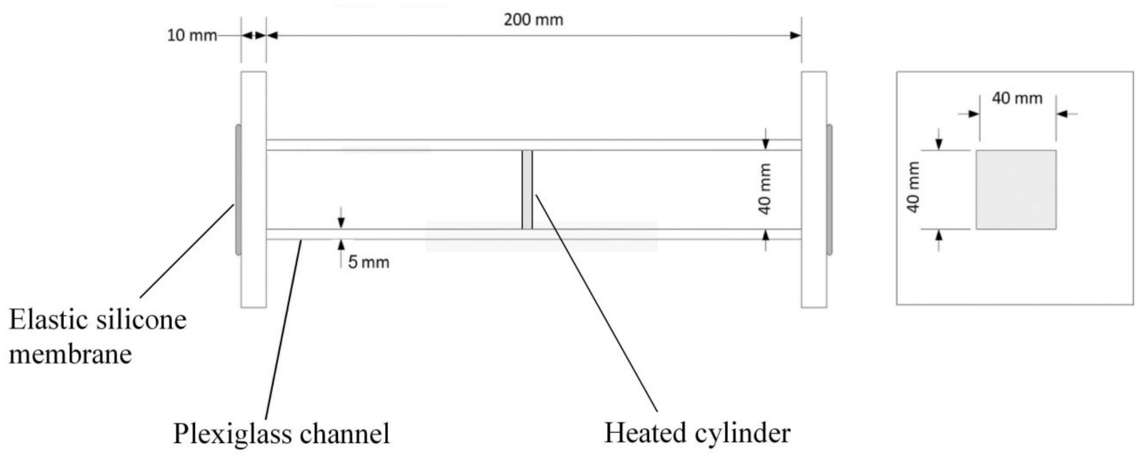

Figure 2.1. Schematic diagram of the water channel.

Single cylinder
D=1.6 and 4 mm

Tandem cylinders 1
l/D=2

Tandem Cylinders 2
l/D=3

Finned tube

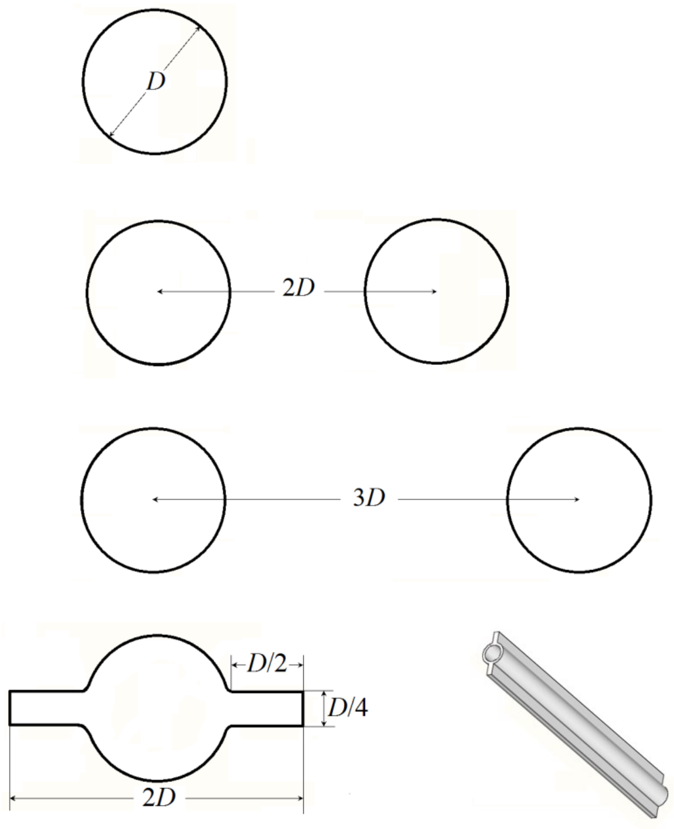

Figure 2.2. Proposed geometries for combined PIV-PLIF measurement. a) single cylinder; b) arrangement of tandem cylinders; and c) finned tube configuration.

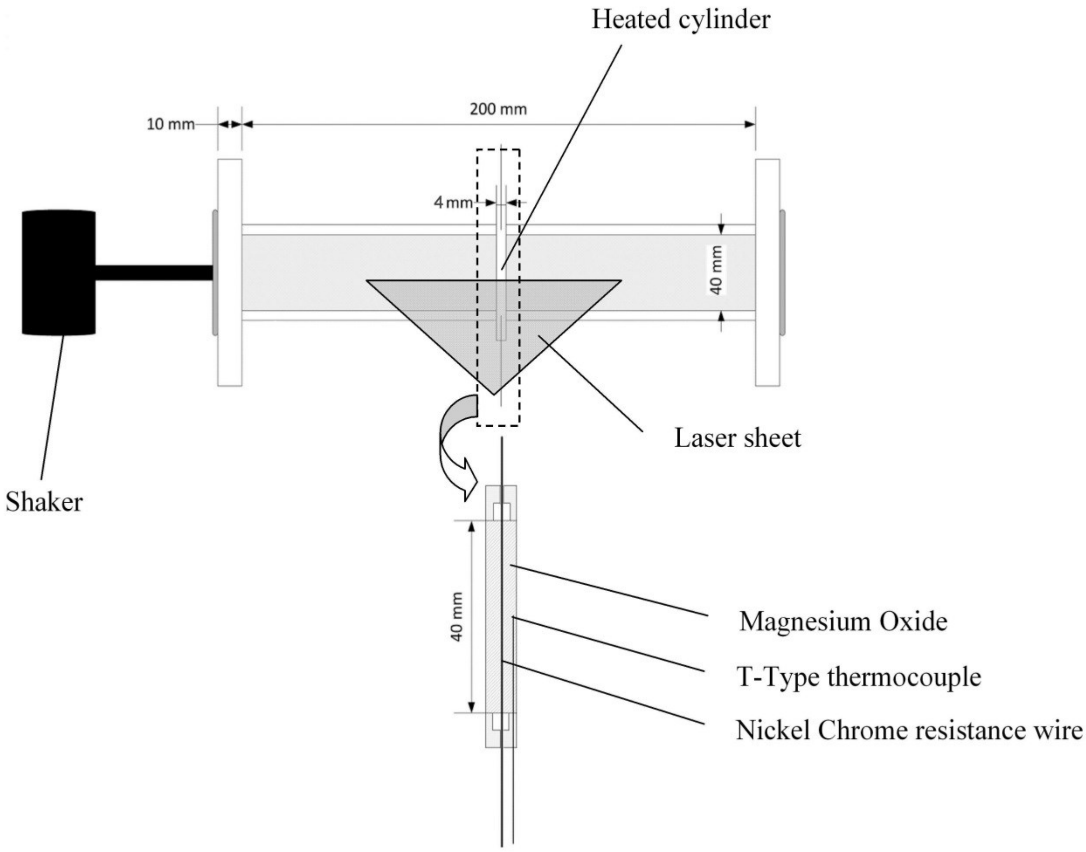

Figure 2.3. Schematic diagram of the test section.

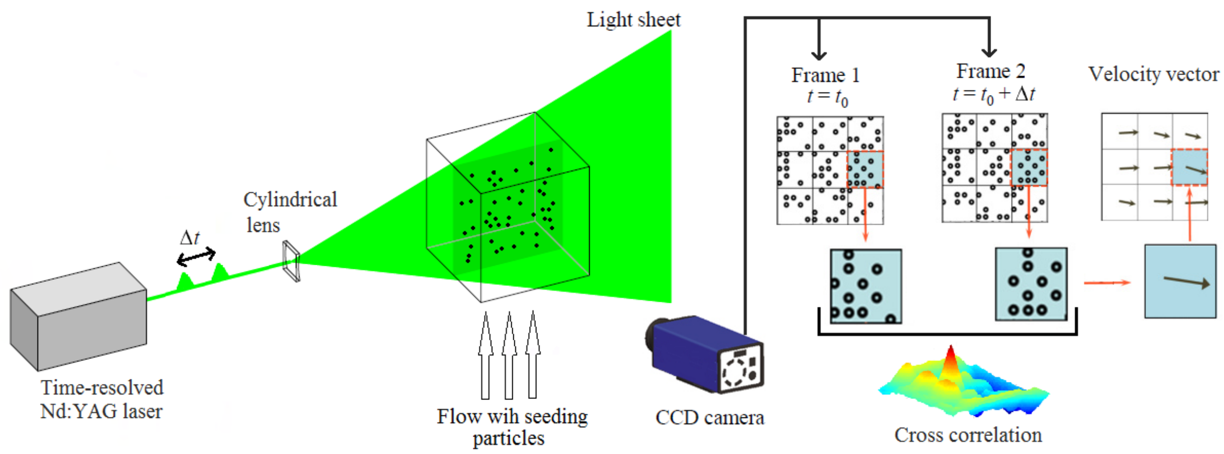

Figure 2.4. Graphical illustration of the PIV principles.

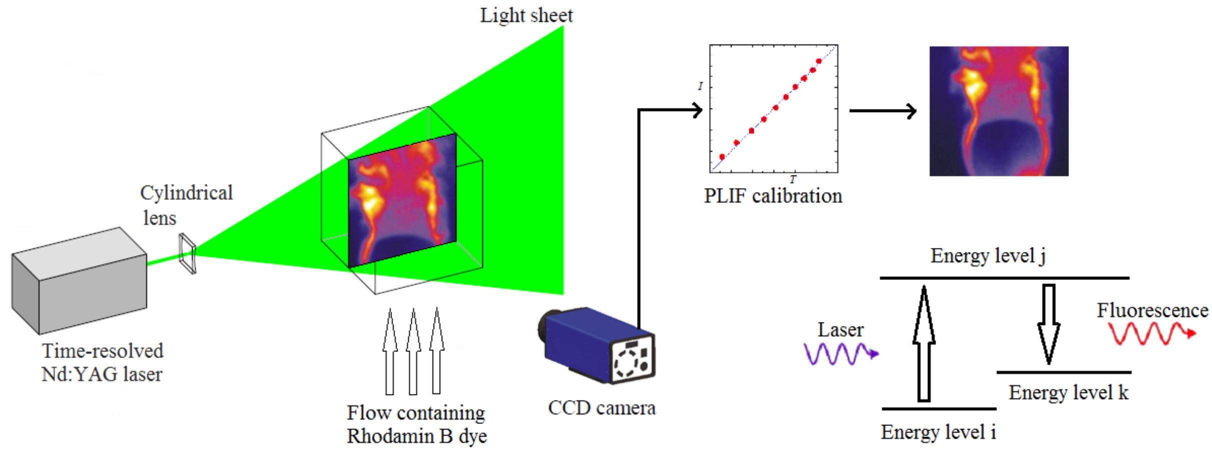

Figure 2.5. Graphical illustration of the PLIF principles.

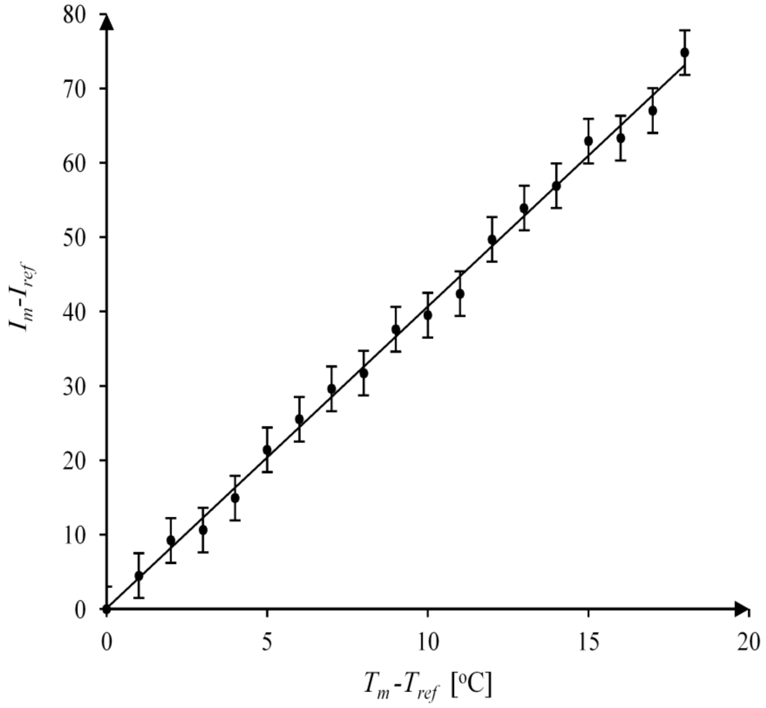

Figure 2.6. Calibration of the PLIF.

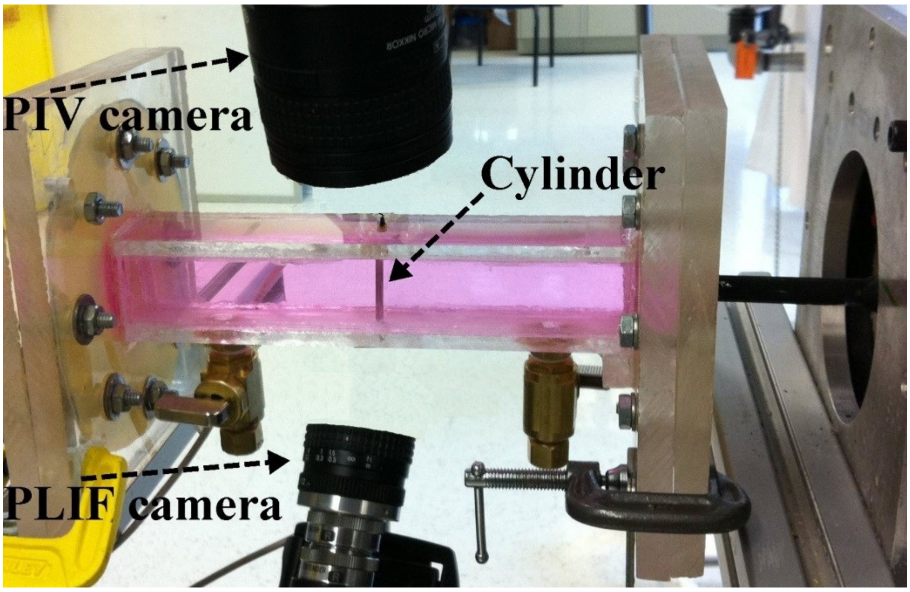

Figure 2.7. Photograph of the experimental apparatus.

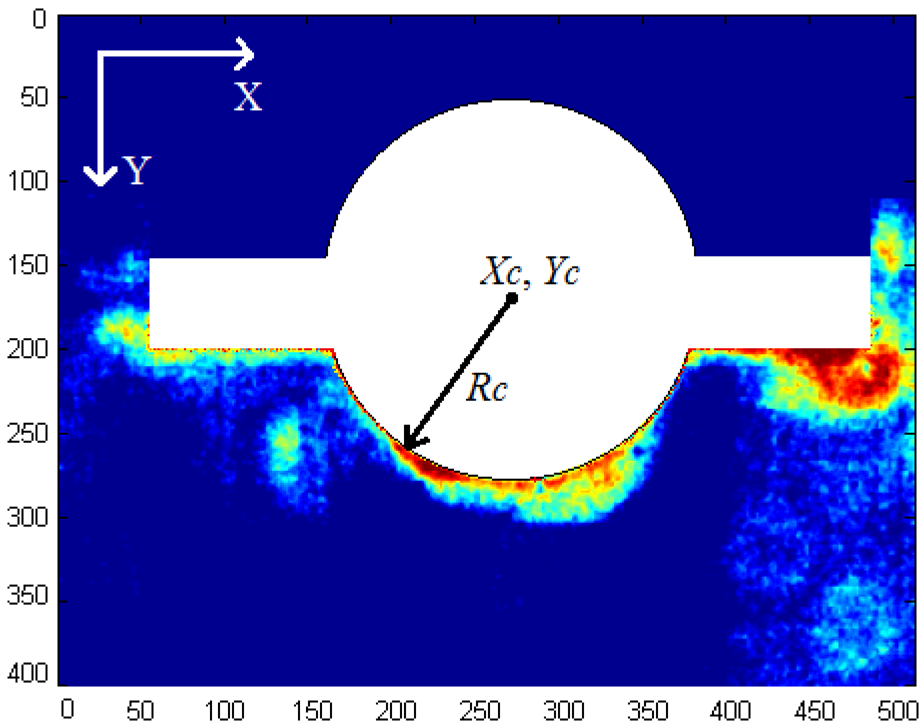

Figure 2.8. Typical PLIF image showing the location of the finned tube bluff body.

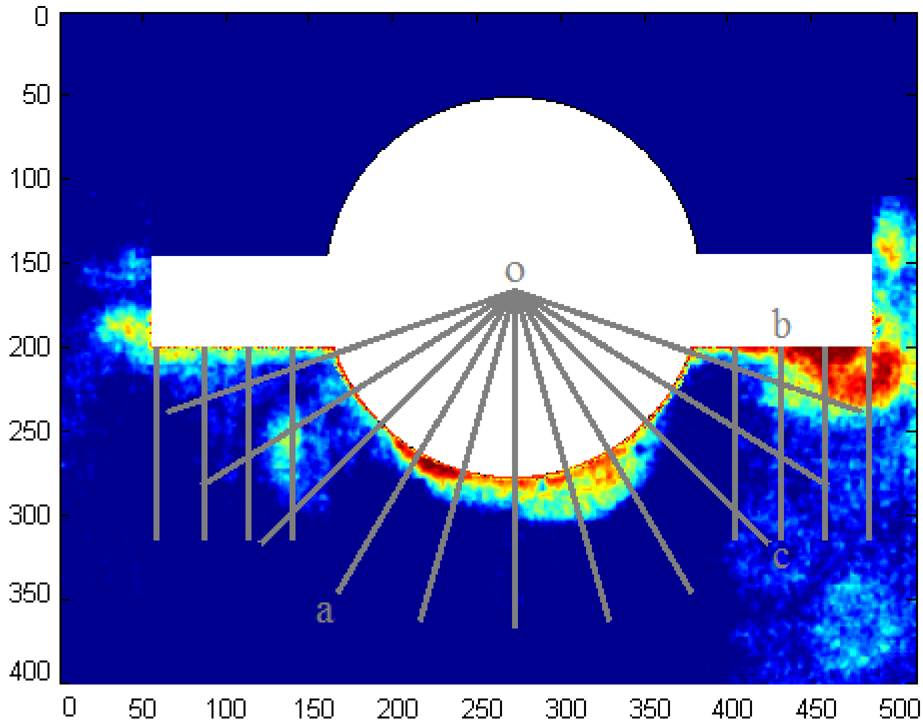

Figure 2.9. Radial and vertical lines to read the pixel intensity.

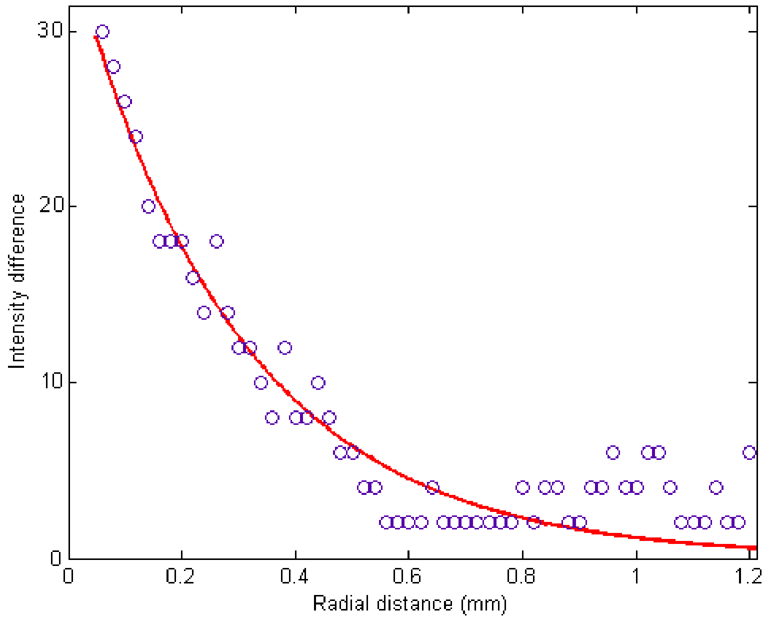

a)

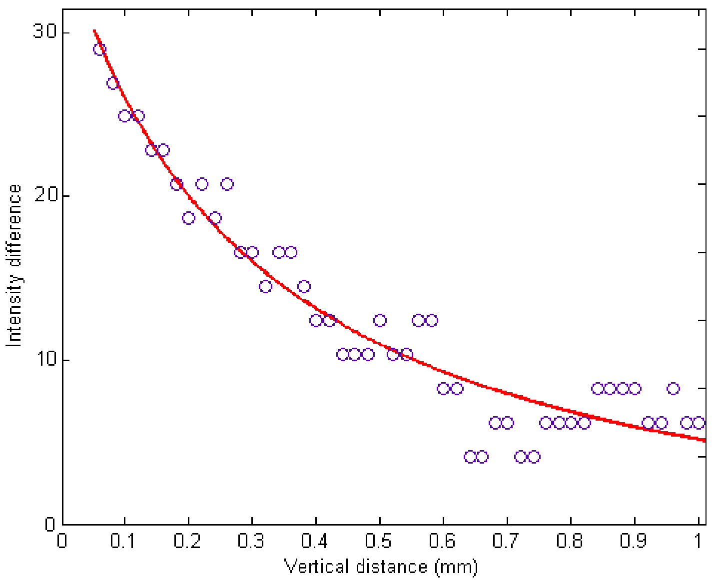

b)

Figure 2.10. Intensity distribution and exponential curve fitting, a) along "o-a", b) along "b-c", ○: Raw data, ___: Exponential curve fitting.

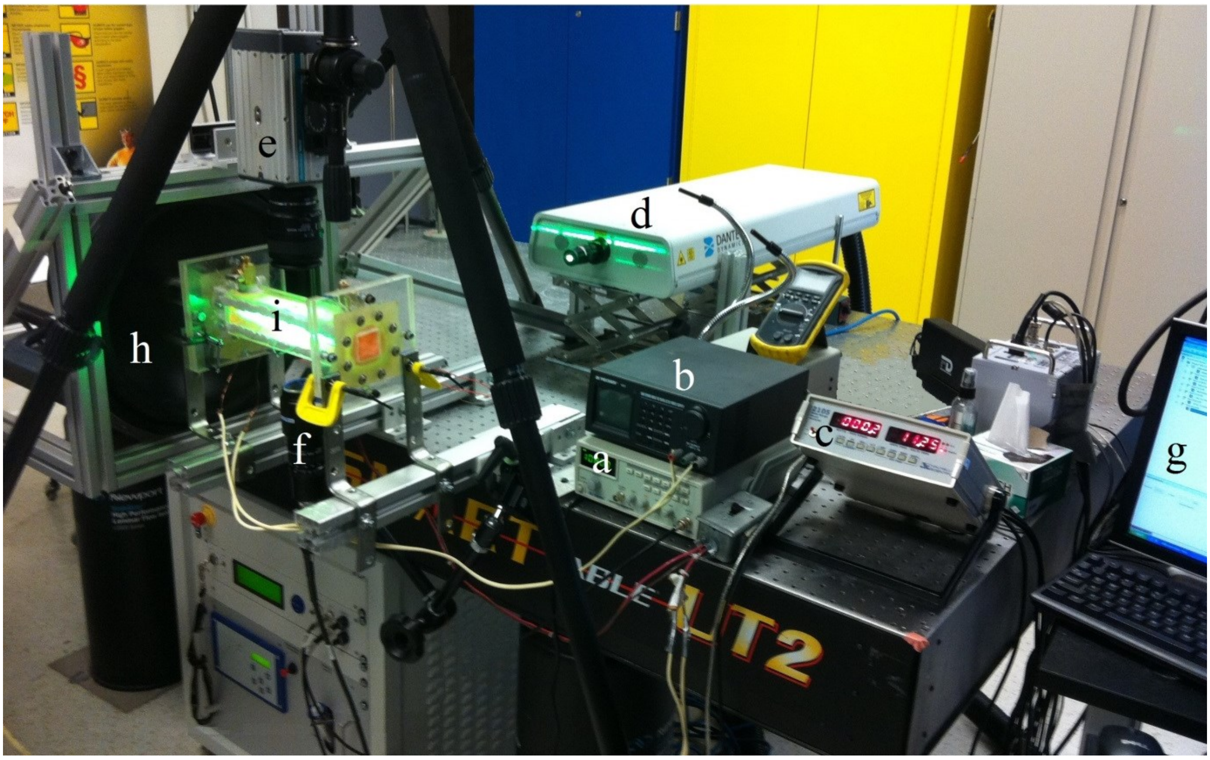

Figure 2.11. Photograph of the experimental apparatus, a) Digital signal generator, b) DC power supply, c) Power analyzer, d) Nd:YLF laser, e) PIV camera, f) PLIF camera, g) Computer, h) Acoustic subwoofer, i) Test section.

Chapter 3

Heat transfer characterization of single circular cylinder in oscillating flow

3.1 Introduction

In the following chapter of this thesis, the flow and heat transfer over a single circular cylinder immersed in zero-mean velocity oscillation flow was investigated. Synchronous PIV and PLIF was used. The PIV data yielded the vortex trajectories, the axial force, and finally the drag and inertia coefficients. The latter values were compared to available data from the literature in order to verify the accuracy of the experiments. The PLIF data yielded time-dependent, space-dependent and total heat transfer rates as a function of the acoustic Reynolds number, the Keulegan-Carpenter number and the dimensionless frequency. Two cylinders with diameters of D=1.6 and 4 mm were used to investigate the reproducibility of the experiments.

3.2 Flow field measurements

The time-dependent velocity of the oscillatory flow, $u(t)$, was defined in terms of the velocity amplitude, U_{max}, as

$$u(t)=U_{max}\sin(\omega t)\,, \tag{3.1}$$

where ω is the oscillation angular frequency. In order to verify the sinusoidal behaviour of the free stream flow, the instantaneous axial component of the free stream velocity, u_x, was measured in a location far away from the cylinder. The velocity time history shown in Fig. 3.1 confirms that the free stream flow is sinusoidal.

3.2.1 PIV visualization

Fig. 3.2 shows the instantaneous flow velocity field around the cylinder. This figure was obtained by line integral convolution processing and was based on corresponding instantaneous velocity-vector fields near the cylinder, sampled at the phases ωt=π, 7π/6, 8π/6, 9π/6, 10π/6, 11π/6, and 2π for the case of KC=6.42, and β=115.

During the first quarter of the cycle ($\pi \leq \omega t \leq 3/2\pi$), flow is accelerating and the cross-sectional mean velocity is greatest at the phase ωt =3/2π. In the second quarter of the cycle ($3/2\pi \leq \omega t \leq 2\pi$), flow is decelerating. The formation of vortices is clearly observed in the decelerating phases on the downstream side (i.e., the left side of the cylinder). Vortices are also formed in the accelerating phases, but not as clearly as the pattern observed in the decelerating phases. Velocity diminishes during the final period of the decelerating phase and at the beginning of the accelerating phase. Therefore, the formation of vortices is decelerated.

Fig. 3.2a and Fig. 3.2g correspond to instants when the cross-sectional mean velocity is zero. At this moment, fluid near the cylinder is not yet quiescent, but it is moving under the action of viscous effects and the flow induced by the vortices. During the acceleration phases, previously shed vortices are convected back to and hover around the cylinder. Each induces a circulating flow around its respective position. This vortex-induced flow affects the formation of new vortices, their positions, and flow motion near the cylinder.

3.2.2 Path of vortex trajectories

The centers of the vortices were identified using the vorticity field and the trajectories were tracked by following the centers of the vortices frame by frame. The vortex trajectories were tracked for KC = 6.42 and β=115 over two successive cycles and are sketched in Fig. 3.3. In this case, there are no major vortices shed during one-half cycle, although two small vortex pairs are formed and are detached from the cylinder as the flow reverses direction. The vortex trajectories can change slightly from one cycle to another. The eddies are washed over the cylinder as the flow is reversed, initiating an interaction with the newly forming eddies on the opposite side of the cylinder. The vortex pair remains close to the cylinder and seems to be dissipated as it is convected back towards the cylinder during flow reversal.

3.2.3 Determination of axial force

The instantaneous axial (along the x direction) force per cylinder unit length, F_x^*, was calculated using the momentum-based approach developed by Unal et al. [38]. This method calculates the force using experimentally based velocity fields (PIV) by considering a control volume around the cylinder. The net rate of momentum change within the control volume and the net momentum flux across the control surface boundaries are computed from the velocity field at each instant during the oscillating motion. A MATLAB script was written to determine the instantaneous axial force in which a control volume was considered around the cylinder. The momentum change within the control volume was calculated by determination of the flow acceleration using two successive instantaneous velocity field data. The time history of the instantaneous axial force, F_x^*, is shown in Fig. 3.4 for KC=3.92 and β=115. The axial force per unit length on an identical cylinder under the equivalent steady flow conditions was added to Fig. 3.4 in order to compare the axial force in steady and oscillating flows. For a steady flow, the axial force is proportional to the velocity square and is increased with an increase in the stream flow velocity. But for an oscillating flow, the variation of axial force with instantaneous velocity is dependent on the flow acceleration as well, which makes it totally different from a steady flow.

The time history of the instantaneous dimensionless (normalized by $0.5\rho DU_{max}^2$) axial force, F_x, is shown in Fig. 3.5 for KC=3.92 and β=115. It can be seen that the dimensionless axial force is nearly sinusoidal because of the inertial forces. The freestream velocity lags behind the force by approximately 90°. The calculated force results are in good agreement with the results reported by Justesen [7].

3.2.4 Drag and inertia coefficients validation

In oscillatory flow it is common to describe the axial force using the Morison equation, as

$$F_x^* = \frac{1}{2}\rho D C_D u|u| + \frac{1}{4}\pi\rho D^2 C_M \dot{u}\,, \tag{3.2}$$

where ρ is the fluid density and C_D and C_M are drag and inertia coefficients. The Fourier averages of C_D and C_M for a cylinder immersed in an oscillating flow are given by Sarpkaya [39] as

$$C_D = \frac{3}{8}\int_0^{2\pi} \frac{F_x^* \sin(\omega t)}{0.5\rho U_{max}^2 D} d(\omega t)\,, \tag{3.3}$$

and

$$C_M = \frac{U_{max}}{\pi^3 f D}\int_0^{2\pi} \frac{F_x^* \cos(\omega t)}{0.5\rho U_{max}^2 D} d(\omega t)\,. \tag{3.4}$$

For KC=3.92 and β= 115, the drag and inertia coefficients are calculated as C_D=1.29 and C_M=2.07, respectively. These values are close to the values reported by Obasaju et al. [5]. They calculated the drag and inertia coefficients as C_D=1.1 and C_M=1.97, respectively for KC=4 and β= 109.

3.3 Temperature field measurements

The results obtained from the PLIF images are described in the following sub-sections. The analysis was performed using ImageJ and MATLAB scripts as described in Chapter 2.

3.3.1 PLIF visualization

The instantaneous temperature field around the circular cylinder for KC=6.42, β=115 is shown in Fig. 3.6. The intermittent behaviour of the flow demonstrated in the acquired sequences shows a strong time dependence and intrinsically unsteady character. It should be noted that in a steady flow, a hot detached vortex move downstream and the surrounding cold fluid sweeps in from the sides to replace it; while in an oscillating flow, the vortices shed in the first half of a cycle are convected back to the cylinder during the second half of the cycle. This means that vortices shed in a previous cycle may not have been cooled down over one oscillation period. This yields to the creation of warm regions close to the cylinder surface. As a result of this warming effect, the heat transfer from the cylinder is not effectively enhanced by convection as much as for a steady flow.

3.3.2 Determination of instantaneous local Nusselt number

Fig. 3.7 shows the distribution of the instantaneous local Nusselt number, Nu_θ, on the cylinder surface sampled at the same phases as those of Fig. 3.2 and Fig. 3.6 at KC=6.42, β=115. The local Nusselt number was calculated as described in section 2.5. The corresponding instantaneous local Nusselt number data is tabulated in Table 3.1.

Fig. 3.7 shows that when the cross-sectional mean velocity is zero, the local Nusselt number is larger around the stagnation points, θ=0° and 180°. This indicates that, even when the cross-sectional mean velocity is zero or quite small, heat may be transferred due to the local fluid motion induced by the vortices, shed in one cycle and then convected back by the reversed flow, while these hover near the cylinder. In other words, the secondary vortex interaction in the oscillatory flow is responsible for the large temperature gradient around the stagnation points. The local Nusselt number has its lowest value all around the cylinder at the end of the accelerating phase. The low heat transfer is caused by the clinging of the hot old vortices around the cylinder, i.e. a local warming effect. Fig. 3.7 shows that the thermal field is nearly periodic since the distribution of Nusselt number at the beginning and end of the half cycle is almost equal.

3.3.3 Determination of spatially-averaged Nusselt number

The spatially-averaged Nusselt number, Nu_{sp}, was calculated by averaging the local Nusselt number over the surface of the cylinder. Fig. 3.8 shows the time history of spatially-averaged Nusselt number during three successive cycles when β=82 and for two values of KC, namely, KC=9.50 and 14.75. It can be observed that the spatially-averaged Nusselt number is fluctuating at twice the excitation frequency. The figure shows that when the KC increases, both the total Nusselt number and the amplitude of spatially-averaged Nusselt number fluctuation increases. The spatially-averaged Nusselt number has an absolute maximum and minimum value over each complete cycle of forced oscillation. The maximum and minimum values, however, change slightly from cycle to cycle. It is noteworthy that the maximum spatially-averaged Nusselt number mostly happens when the flow is at both ends of the stroke. This happens because small and weak vortices mainly form at the end positions of the oscillating motion. Thus, local fluid motion induced by the vortices around the cylinder increases. The vortex motion near the cylinder surface increases heat convection since it brings low temperature fluid close to the surface, causing a large temperature gradient.

3.3.4 Determination of total Nusselt number

The total Nusselt number, Nu_{tot}, was determined as described in section 2.5 of this thesis. Fig. 3.9 shows a comparison between the measured total Nusselt number obtained in this study and the data reported by Mozurkewich [24] and Paek et al. [25]. Mozurkewich's experimental results were obtained from an array of tubes made of aluminum over the frequency range of 205-460 Hz; in the present study, the operating frequency was kept between 7 to 35 Hz. According to Mahfouz and Badr [40], heat transfer increases with an increase in frequency. This may explain the lower Nu_{tot} measured in the present study compared with the higher Nu_{tot} reported by Mozurkewich. In Paek et al.'s study, the heat exchanger had brazed aluminum construction with folded fins; while in the present chapter, the cylinder had no fins. The fins increase the heat transfer surface area and subsequently the heat transfer rate. This probably explains why the heat transfer rate measured in this study is smaller than that reported by Paek et al.

3.3.5 Colburn-j factor correlation

The results are presented in terms of Colburn-j factor, j_H, defined as

$$j_H = StPr^{\frac{2}{3}} = \frac{Nu_{tot}}{Re_{ac}\, Pr^{\frac{1}{3}}}, \tag{3.5}$$

where *St* and *Pr* are the Stanton and Prandtl numbers, respectively. The Colburn-j factor enables the collapse of heat transfer data for different Prandtl numbers into one single curve. Fig. 3.10 shows the variation of Colburn-j factor with respect to the acoustic Reynolds number. The measured data was compared to the data reported by Paek et al. [25]. The solid line is a regression obtained for the measured data. The resulting correlation yields the expression

$$j_H = 0.3480 Re_{ac}^{-0.5292} . \tag{3.6}$$

The R-squared value of the regression curve was 0.977. The Colburn-j factor was reduced by increasing the acoustic Reynolds number. The measured data showed a trend similar to Paek et al.'s results, but the values of measured Colburn-j factor were slightly different due to the different test section configurations.

3.4 Reproducibility of results

The ability to get consistent results after changing the geometrical and flow parameters is defined here as reproducibility of the experimental data. In order to verify this, cylinders with two different diameters were used. The outer diameter of the first cylinder was D=1.6 mm and the second cylinder outer diameter was D=4 mm. The detailed specifications of these cylinders are provided in Table 2.1. The total Nusselt number obtained for the verification of the data reproducibility tabulated in Table 3.2 and illustrated in Fig. 3.11. For the acoustic Reynolds number within the range between $492 < Re_{ac} < 1536$, the standard deviation of $Nu \times Pr^{-0.37}$ for the first and second sets of experiments are 1.50 and 2.19, respectively. The blockage ratios for the first and second sets were 25 and 10, respectively. This may explain the higher standard deviation calculated for the second set. Variation of total Nusselt number shows a similar trend and magnitude for both cases. It can be deduced from the results that our experimental data is reproducible.

3.5 Conclusion

Flow and heat transfer near the surface of a single circular cylinder immersed in a sinusoidal velocity oscillating flow was investigated. Simultaneous measurements of the flow velocity and temperature fields were performed using combined PIV-PLIF technique. Vortex trajectories were tracked and the axial force, the drag and the inertia coefficients were determined and compared to values reported in the literature. The detailed heat transfer characteristics around the cylinder were obtained in terms of instantaneous local Nusselt number. The reproducibility of the experiments was confirmed. The intermittent, time-varying vortex shedding behaviour of the flow, demonstrated in the image sequences, showed a strong time dependence and a naturally unsteady character. The results showed that heat transfer can be enhanced due to the local fluid motion induced by the vortices around the cylinder, entrained away and by the forwarded reverse flow. This heat transfer enhancement was countered by the local warming effect of the hot vortices clinging to the cylinder.

Table 3.1. Distribution of the instantaneous local Nusselt number for *KC*=6.42, *β*=115.

	Angular location																		
Phase	**θ=0**	**θ=10**	**θ=20**	**θ=30**	**θ=40**	**θ=50**	**θ=60**	**θ=70**	**θ=80**	**θ=90**	**θ=100**	**θ=110**	**θ=120**	**θ=130**	**θ=140**	**θ=150**	**θ=160**	**θ=170**	**θ=180**
$\omega t=\pi$	7.00	8.24	8.52	9.71	10.02	11.63	13.28	13.79	13.83	14.32	14.38	12.95	13.72	14.67	15.90	17.68	22.71	27.31	29.15
$\omega t=7\pi/6$	9.11	9.60	9.49	9.09	11.60	13.25	14.38	14.25	13.46	12.91	12.69	13.14	13.56	14.37	15.41	16.19	17.67	19.14	24.35
$\omega t=8\pi/6$	5.70	5.96	5.65	6.23	7.88	9.48	10.11	10.57	10.17	9.86	9.39	9.41	9.98	10.80	11.49	12.01	12.05	13.70	14.52
$\omega t=9\pi/6$	12.39	11.76	10.14	8.53	8.27	8.51	8.23	10.00	10.32	10.46	10.05	9.49	9.30	9.38	9.22	8.43	7.06	7.06	6.50
$\omega t=10\pi/6$	21.91	20.46	20.35	19.45	18.60	15.41	12.96	9.84	7.46	6.32	6.97	7.22	8.40	9.33	9.54	8.45	7.84	7.44	7.94
$\omega t=11\pi/6$	31.10	29.39	26.81	23.24	22.95	20.72	18.82	16.96	14.44	14.68	13.41	13.63	13.33	12.85	11.74	10.68	9.10	8.59	8.62
$\omega t=2\pi$	34.79	33.14	30.66	26.71	23.83	18.50	16.51	14.75	13.43	11.89	10.33	9.10	9.14	8.74	8.27	8.04	7.35	7.60	7.17

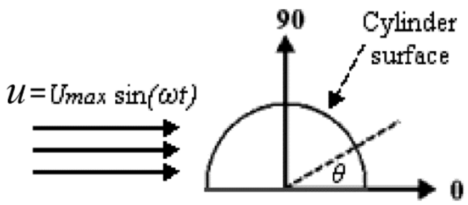

Table 3.2. Variation of $Nu \times Pr^{-0.37}$ vs. acoustic Reynolds number.

	Acoustic Reynolds number, Re_{ac}												
	492	**553**	**737**	**778**	**901**	**983**	**1127**	**1210**	**1372**	**1476**	**1536**	**1968**	**2460**
Set 1	---	6.50	7.03	7.60	8.08	8.25	8.88	8.74	9.32	---	9.99	---	---
Set 2	6.04	---	---	---	---	8.92	---	---	---	10.33	---	12.51	13.07

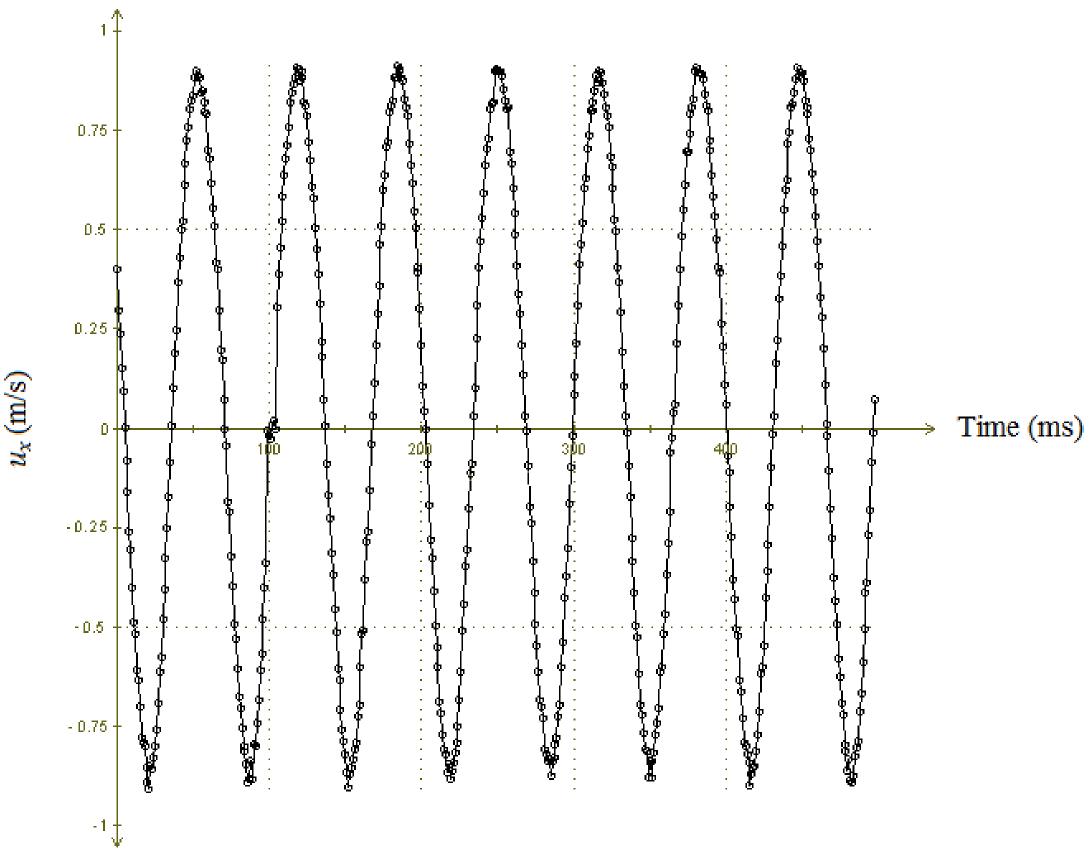

Figure 3.1. Time history of the axial component of the free stream velocity.

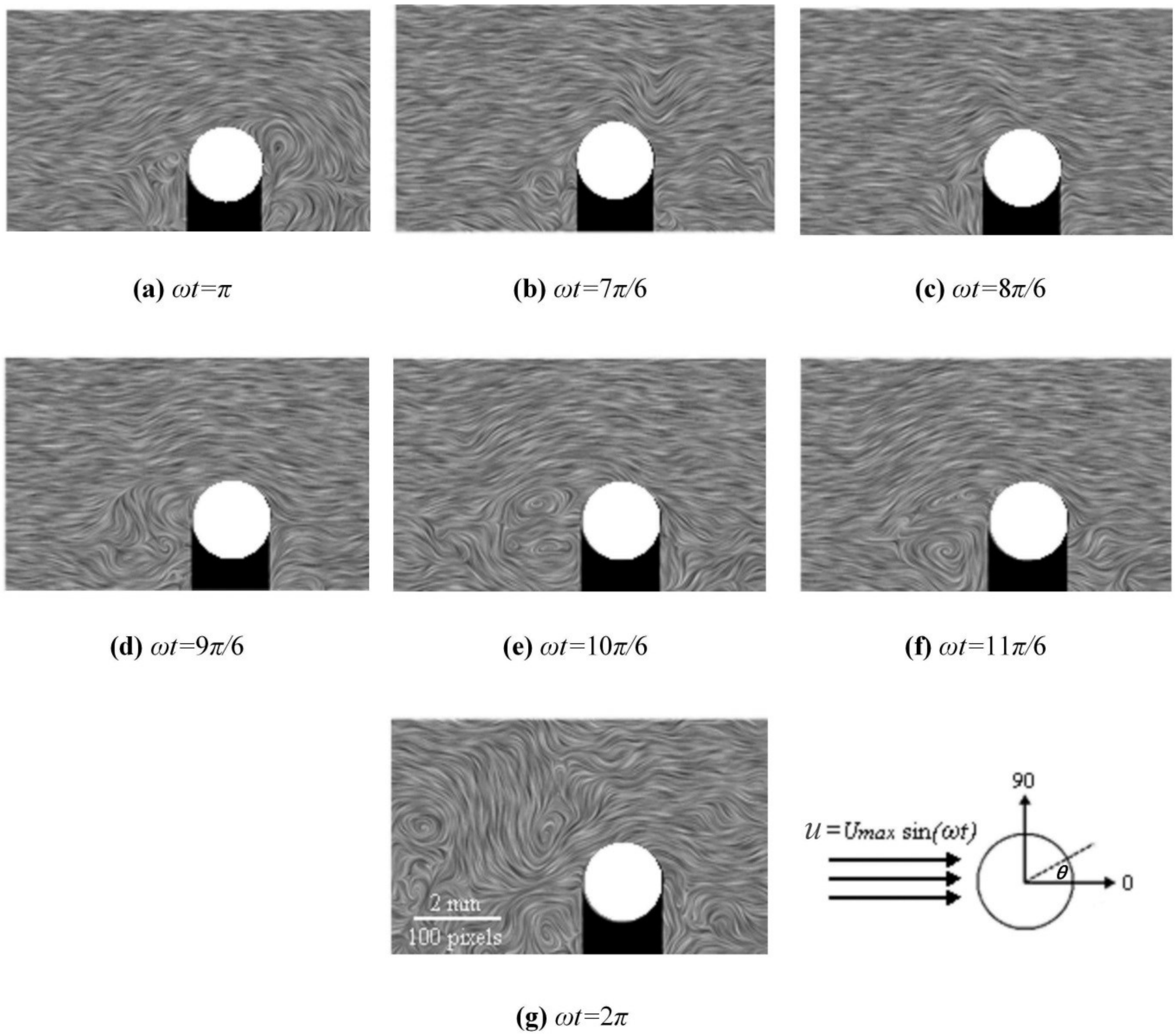

Figure 3.2. Time history of line integral convolution contours around the cylinder during a half cycle at KC=6.42, β=115, (a) to (g) correspond to $\omega t = \pi$, $7/6\pi$, $8/6\ \pi$, $9/6\ \pi$, $10/6\ \pi$, $11/6\ \pi$ and 2π, respectively.

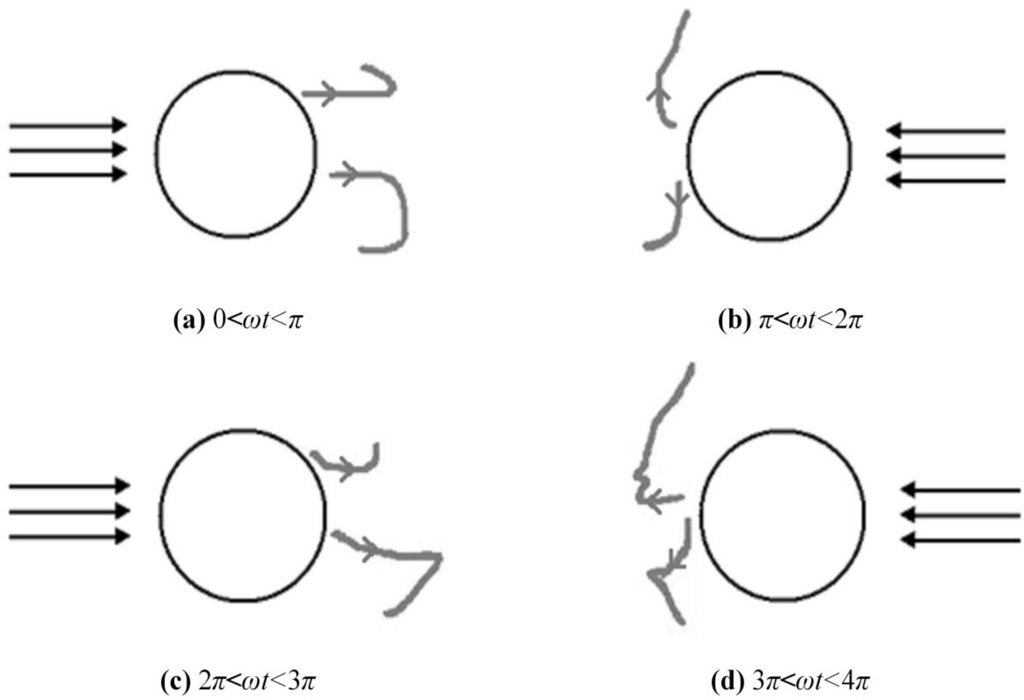

Figure 3.3. Vortex trajectories during two successive cycles at KC = 6.42 and β=115.

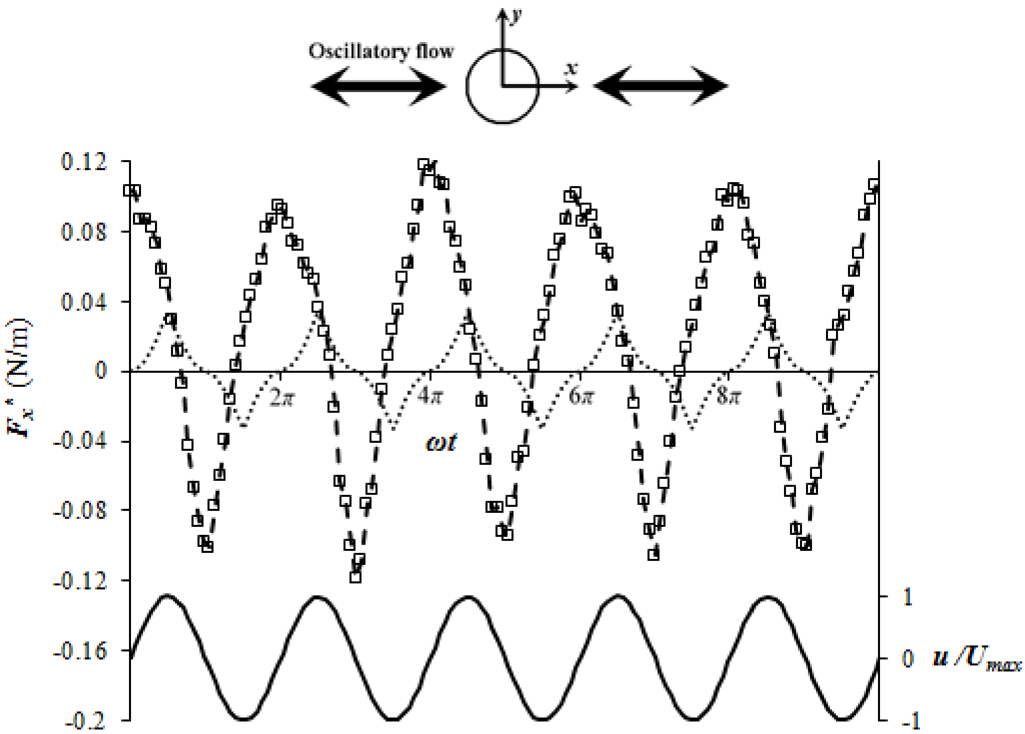

Figure 3.4. Time history of axial force per cylinder unit length over five periods of oscillation for KC=3.92 and β=115, ---□---: Axial force for the oscillating flow, ….: Axial force for the equivalent steady flow, ——: Free stream velocity.

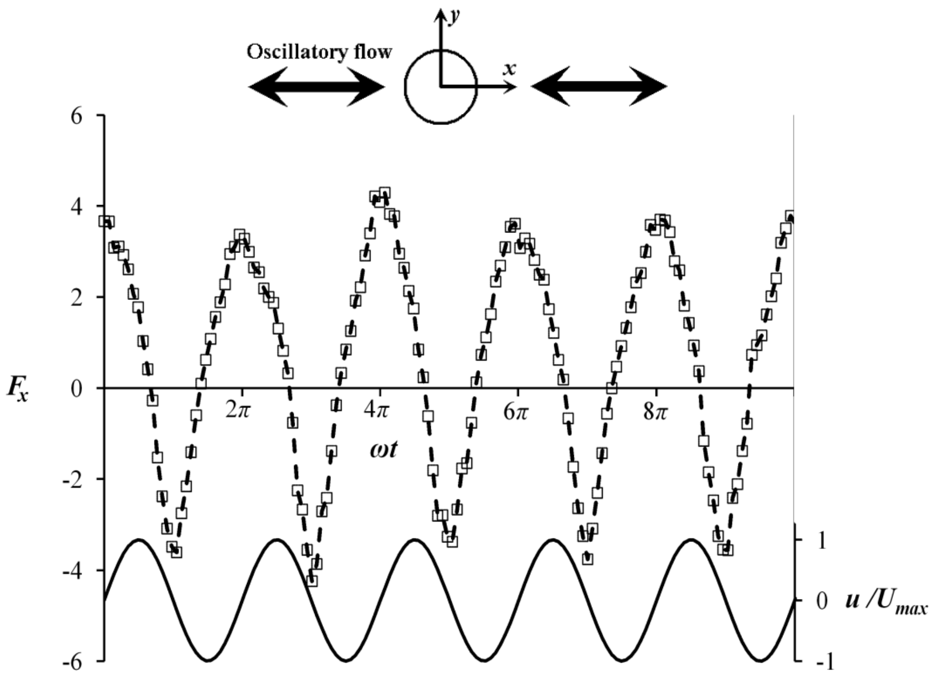

Figure 3.5. Time history of dimensionless axial force over five periods of oscillation for *KC*=3.92 and *β*=115, ---□---: Dimensionless axial force, ——: Free stream velocity.

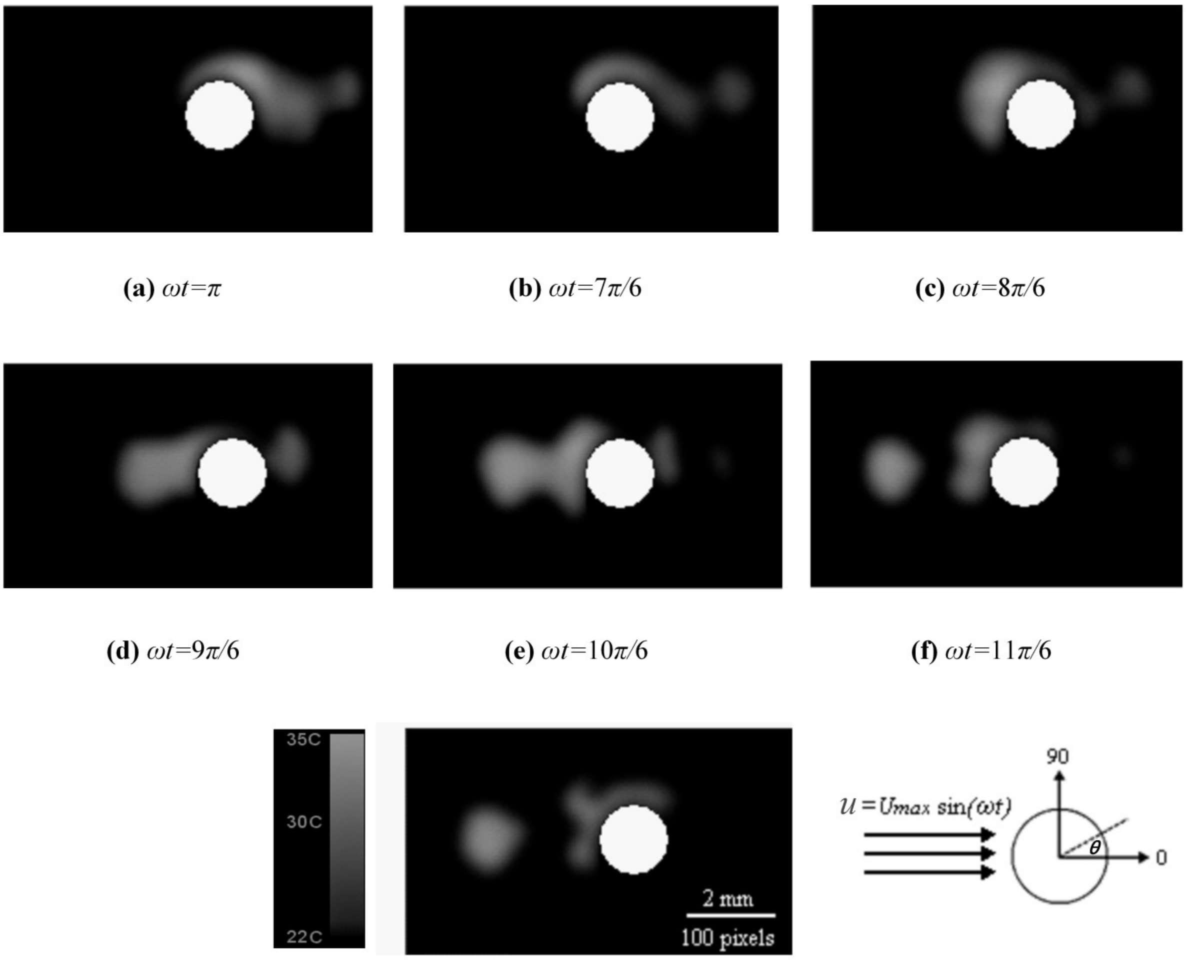

(a) $\omega t=\pi$ **(b)** $\omega t=7\pi/6$ **(c)** $\omega t=8\pi/6$

(d) $\omega t=9\pi/6$ **(e)** $\omega t=10\pi/6$ **(f)** $\omega t=11\pi/6$

(g) $\omega t=2\pi$

Figure 3.6. Time history of temperature field around the cylinder during one-half cycle at *KC*=6.42, β=115, (a) to (g) correspond to ωt = π, $7/6\pi$, $8/6\ \pi$, $9/6\ \pi$, $10/6\pi$, $11/6\pi$ and 2π, respectively.

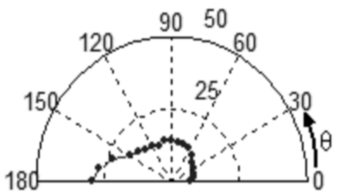

(a) $\omega t=\pi$

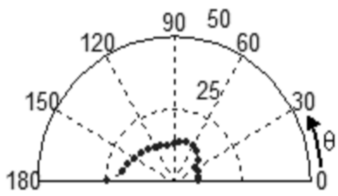

(b) $\omega t=7\pi/6$

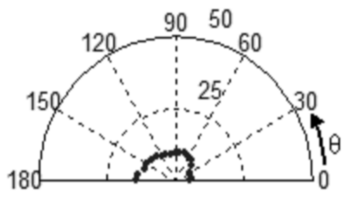

(c) $\omega t=8\pi/6$

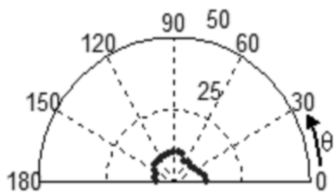

(d) $\omega t=9\pi/6$

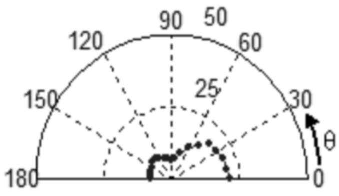

(e) $\omega t=10\pi/6$

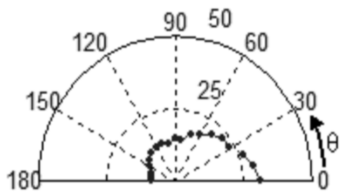

(f) $\omega t=11\pi/6$

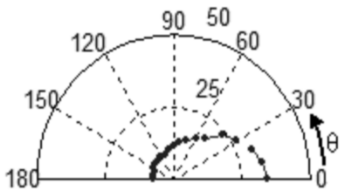

(g) $\omega t=2\pi$

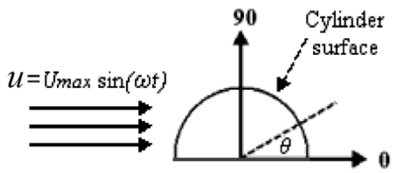

Figure 3.7. Time history of instantaneous local Nusselt number, Nu_θ, at KC=6.42, β=115, (a) to (g) correspond to $\omega t = \pi$, $7/6\pi$, $8/6\ \pi$, $9/6\ \pi$, $10/6\ \pi$, $11/6\ \pi$ and 2π, respectively.

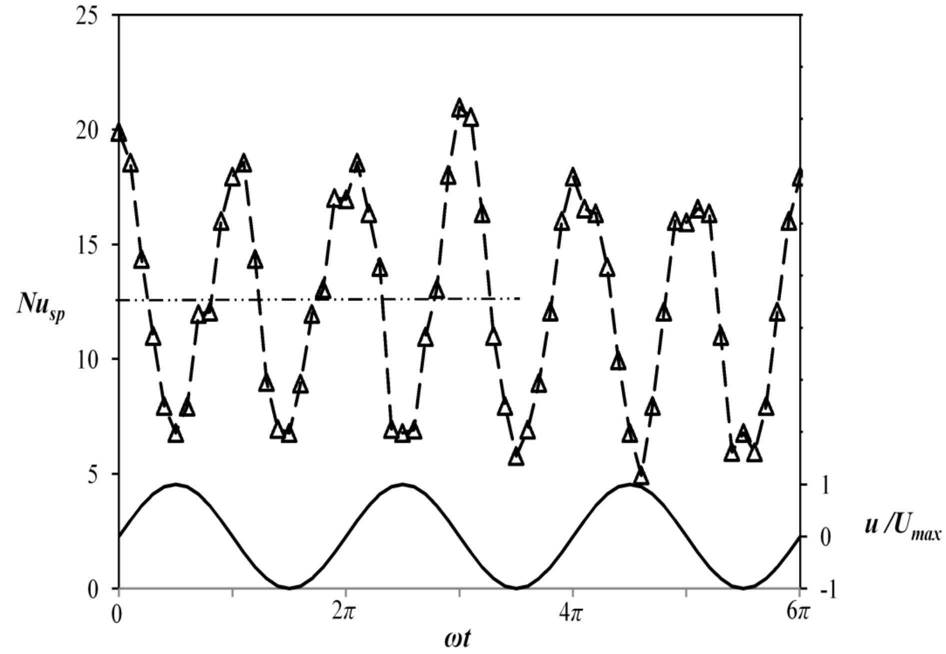

a) *KC*=9.50

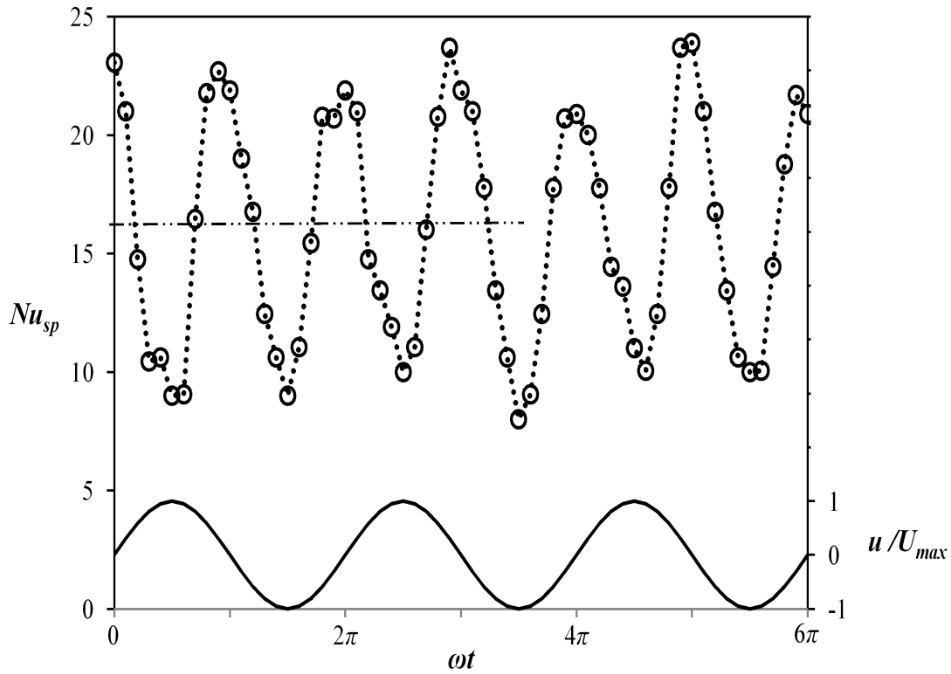

b) *KC*=14.75

Figure 3.8. Time history of space-averaged Nusselt number during three successive cycles for β=82, --Δ--: Spatially-averaged Nusselt number at *KC*=9.50, --○--: Spatially-averaged Nusselt number at *KC*=14.75, - • • -: Total Nusselt number, ——: Free stream velocity.

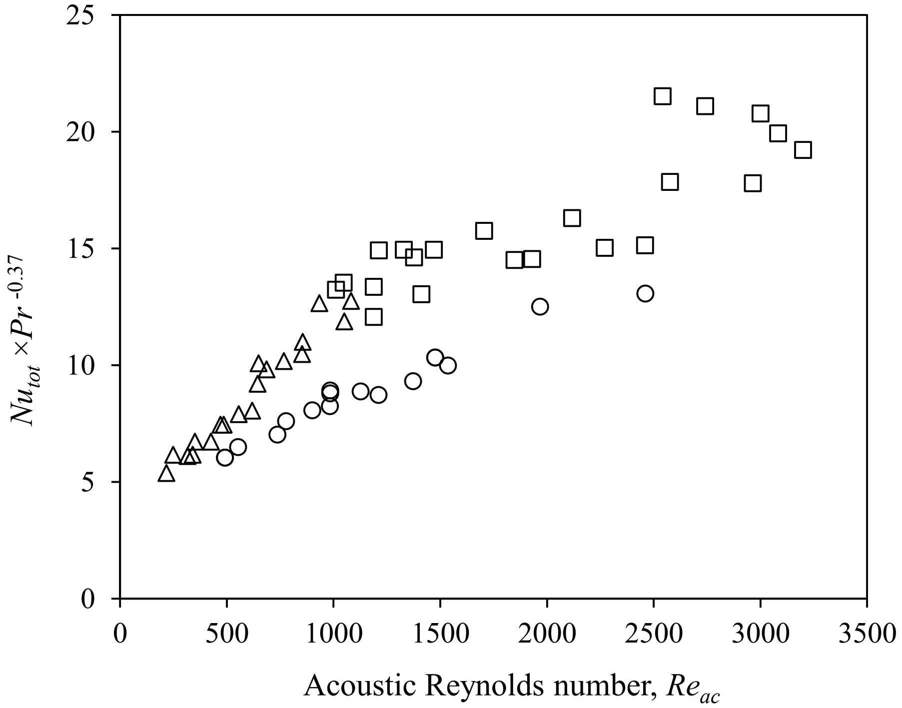

Figure 3.9. Total Nusselt number vs. acoustic Reynolds number, ○: Measured data, Δ: Mozurkewich data [24], □: Paek et al. data [25].

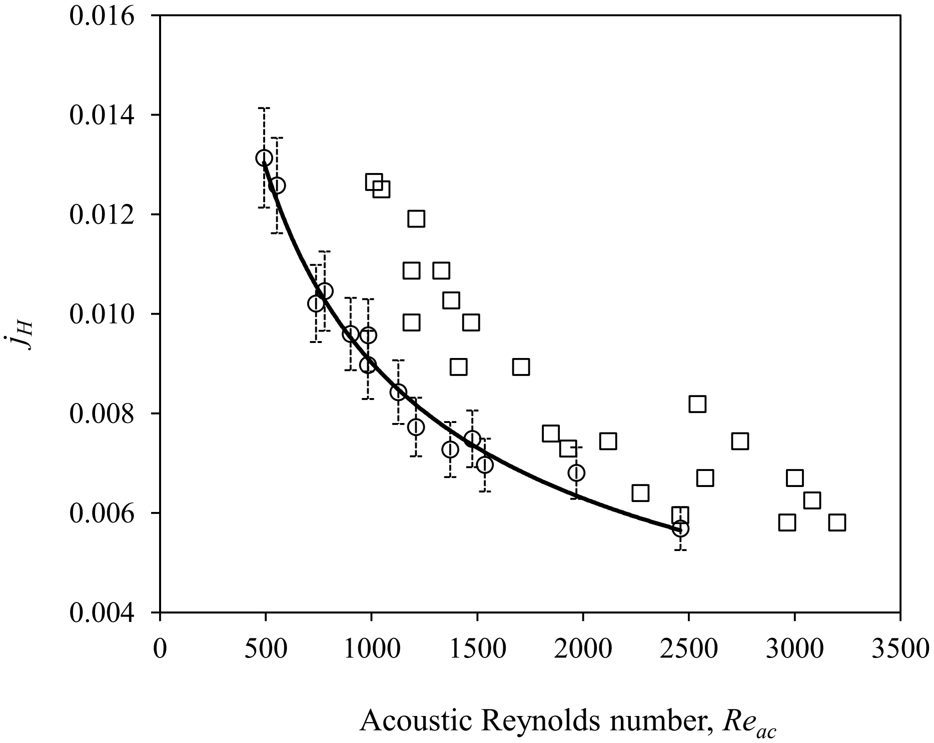

Figure 3.10. Colburn-j factor vs. acoustic Reynolds number, ○: Measured data, ____: Regression curve of the measured data, □: Paek et al. data [25].

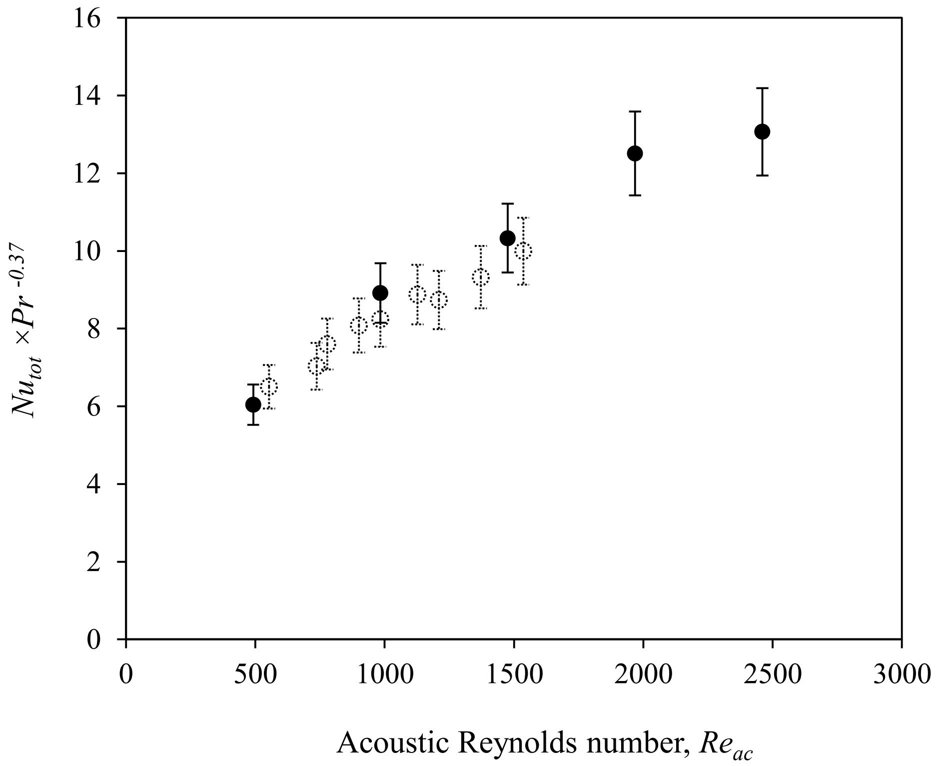

Figure 3.11. Total Nusselt number vs. acoustic Reynolds number for verification of the reproducibility of the experiments, ○: set 1 (D=1.6 mm), ●: set 2 (D=4 mm).

Chapter 4

Heat transfer characterization of tandem cylinders in oscillation flow

4.1 Introduction

In heat exchangers, the orientation of the cylinders with respect to the direction of the free stream flow can be tandem (in-line) or side-by-side (transverse). In side-by-side arrangements, the flow and heat transfer around both cylinders are similar to those for a single cylinder under identical conditions. Whereas in tandem arrangements, the flow and heat transfer around the downstream cylinder is highly affected by the presence of the upstream cylinder. The complexity of such a flow and thermal field was the motivation for the experiments described in this chapter.

4.2 Description of the experiment

Fig. 4.1 shows the configurations of the tandem cylinders for center-to-center distance to diameter ratio l/D=2 and 3. Two identical cylinders with D=4 mm were vertically mounted in the water channel. Preliminary tests were performed to verify that each cylinder experienced the same surface temperature under identical input electrical power. In order to heat both the cylinders with the same power, they were connected to the DC power supply using parallel wiring. Two different center-to-center to diameter ratios l/D=2 and 3 were examined to investigate the effects of cylinder spacing on heat transfer. The sinusoidal signal was fed into the amplifier from a digital signal generator and the sinusoidal oscillatory motion was imposed using an acoustic subwoofer. The displacement amplitude of fluid particle were chosen to change within the range of $D/2 < A_{max} < 5D/2$. As for the single cylinder case, synchronous

PIV-PLIF measurements were performed to capture the flow and thermal fields simultaneously. The PIV and PLIF cameras were synchronized and captured the flow and thermal field with a frame rate of 1000 fps.

4.3 Flow field measurements

For PIV measurements, images were captured with a resolution of 1280×1024 pixels. Each pixel had a pitch of 38 μm. A new set of calibration test was performed before the final experiments to determine the camera lens magnification factor.

4.3.1 PIV visualization

In contrast with isolated cylinders, the flow around cylinder in a tandem configuration is modified due to hydrodynamic interference. The velocity vector map of the flow is shown in Fig. 4.2 for different phases during one oscillating cycle at KC=3.14, β=158.1 and l/D=2. For this case, the velocity amplitude was U_{max}=0.09 m/s which corresponds to the Figs. 4.2(c) and 4.2(g). The fluid particles in the region between two cylinders were observed to have a small axial displacement compared to the flow displacement amplitude (A_{max}) during one oscillation cycle. In other words, the fluid particles were blocked inside that region due to oscillating nature of the free stream flow and observed to have a chaotic motion.

The hydrodynamic interference effects were found to be greater for the downstream cylinder compared to the upstream cylinder. Vortex shedding was not observed from the upstream cylinder for none of the cylinder spacing l/D=2 and 3. In other words, for the mentioned distances, the wake was formed as though it was created by a single large bluff body. However, a small weak attached vortex pair was observed behind the downstream cylinder. The flow interference had significant effects on the induced axial force on the downstream cylinder, as discussed quantitatively in the next section.

4.3.2 Determination of axial force

The time history of the instantaneous dimensionless (normalized by $0.5\rho DU_{max}^2$) axial force, F_x, is shown in Fig. 4.3 for KC=3.14, β=158.1 and L/D=2over three periods of oscillation. This plot shows the time history of the force on the left-hand side cylinder. The instantaneous axial force, F_x^*, was calculated using a MATLAB script as described in Chapter 3. During the first half of one cycle ($0 \leq \omega t \leq \pi$), the fluid particles moved in the right direction and the left-hand cylinder was located upstream of the right-hand cylinder. The axial force on the left-hand side cylinder was similar to that of one isolated cylinder under identical conditions. During the second half of the same cycle ($\pi \leq \omega t \leq 2\pi$), the fluid particles moved in the left direction and the left-hand side cylinder was located downstream of the right-hand cylinder. The downstream cylinder was then within the wake of the upstream one, and consequently experienced a force roughly five times lower than the isolated cylinder.

4.4 Temperature field measurements

Temperature values were inferred from post processing of the PLIF images. In order to maximize the resolution of the captured pictures, the PLIF camera was focused on one cylinder. This allowed a pixel pitch of 20 μm, i.e. between 3-4 pixels inside the thermal penetration depth depending on the oscillation frequency.

4.4.1 PLIF visualization

The time history of the temperature field around the left-hand side cylinder during one oscillating cycle is shown in Fig. 4.4 at KC=3.14, β=158.1 and l/D=2. Near the end of the first half cycle, ($\omega t = \pi$), the thickness of the thermal boundary layer on the stagnation point of the left-hand side cylinder was observed to be minimum, which corresponds to the highest heat transfer rate. The heat transfer rate is further discussed in the next section.

The temperature of the free stream flow was 22 °C. The temperature of the fluid particles in the region between the two cylinders was the greatest within the captured temperature field. Recalling the discussion in section 4.3.1, the displacement of these particles was lower than the displacement amplitude of the free stream flow. As a result, the contribution of these particles to remove the heat from the surface of the cylinders was the lowest. During the first half of the cycle ($0 \leq \omega t \leq \pi$), the left-hand side cylinder temperature field was similar to that of an isolated cylinder subjected to an oscillatory flow, whereas during the second half of the cycle ($\pi \leq \omega t \leq 2\pi$), a complex thermal field was detected around the cylinder. The thermal field around tandem cylinders was observed to be essentially the same for both center-to-center to diameter ratios of l/D= 2 and 3. The only difference was a higher temperature drop in the gap region between the cylinders for l/D=3 compared to l/D=2. This is because when the gap between cylinders increases, the displacement of the fluid particle in the gap region increases, causing a higher local velocity and a lower temperature within that region.

4.4.2 Determination of instantaneous local Nusselt number

The distribution of the instantaneous local Nusselt number, Nu_θ, on the left-hand side cylinder is shown in Fig. 4.5 for KC=3.14, β=158.1 and l/D=2, for the same phases as those of Fig. 4.2 and Fig. 4.4. The method of calculation of the local Nusselt number was described in section 2.5. The corresponding instantaneous local Nusselt number data is tabulated in Table 4.1.

The maximum value of the instantaneous local Nusselt number was observed during the second quarter of the oscillation cycle ($\pi/2 \leq \omega t \leq \pi$), when the flow was decelerating. The largest contribution to the heat transfer from the surface of the cylinders was along the circumference angles between $110 < \theta < 150$. The variation of the instantaneous local Nusselt number was not symmetric during the first and second half of the cycle, compared to that of an isolated single cylinder subjected to a comparable oscillatory flow. There is no stagnation point with high heat transfer on the right-hand side of the cylinder during the second half of the cycle. This resulted in a lower amount of heat transfer during the second half cycle compared to the first half cycle.

4.4.3 Determination of spatially-averaged Nusselt number

Fig. 4.6 shows the time history of spatially-averaged Nusselt number during three successive cycles at KC=3.14, β=158.1 and l/D=2. It was calculated by averaging the local Nusselt number over the cylinder surface. Spatially-averaged Nusselt number values fluctuated in the same way as the excitation frequency of the oscillating flow, and exhibited a double hump. In other words, it underwent through two maxima over one cycle. The absolute maximum value occurred during the first half of the cycle ($\omega t \approx \pi/2$) with a relative maximum extremum observed during the second half cycle ($\omega t \approx 3\pi/2$). Two minima were identified during each complete oscillation periods at $\omega t \approx 0$ and $\omega t \approx 2\pi$ when the velocity of the stream flow was zero.

The upstream cylinder heat transfer was greater than that for the downstream cylinder. Both cylinders exhibited lower heat transfer than that for an isolated single cylinder under similar inflow conditions. When the cylinder spacing was increased from l/D=2 to l/D=3, a higher value for Nusselt number was detected for both cylinders under a given Re_{ac} number. The hydrodynamic interference was thus reduced by increasing the gap between the two cylinders. The increase of Nusselt number was observed to be greater for the downstream cylinder than for the upstream cylinder.

4.4.4 Determination of total Nusselt number

The measured values of the total Nusselt number are shown in Fig. 4.7 for the two cylinder spacings of l/D=2 and 3, and are tabulated in Table 4.2 and Table 4.3. It was observed that in all the studied conditions, the total Nusselt number values increased with an increase in Keulegan-Carpenter number, KC, and Frequency parameter, β. In other words, the heat transfer coefficient increased with an increase in flow displacement amplitude, A_{max}, and oscillation frequency, f.

The effect of the frequency parameter was found to be larger at higher KC numbers. At a given frequency parameter β, the trend of the variation of total Nusselt number with KC number curves was slightly downward. This is reasonable because greater KC numbers indicate higher fluid particle displacements. In other words, the oscillating flow behaves similar to a steady flow at higher KC numbers. These characteristics were observed for both cylinder spacings l/D=2 and 3. In addition, the total Nusselt number for the cylinder spacing l/D=3 was found to be between 8-15 percent greater than that for cylinder spacing l/D=2, depending on the KC and β values.

4.4.5 Colburn-j factor correlation

The variation of the Colburn-j factor with respect to the acoustic Reynolds number is shown in Fig. 4.8. The Colburn-j factor for a cylinder spacing of l/D=3 was found to be greater than that for the cylinder spacing l/D=2 at a given Re_{ac}. The results as shown in Fig. 4.8 are expressed using the following correlations as

for l/D=2: $$j_H = 0.2978 Re_{ac}^{-0.562}, \tag{4.1}$$

and

for l/D=3: $$j_H = 0.3017 Re_{ac}^{-0.549}. \tag{4.2}$$

The R-squared values of the regression curves were 0.9932 and 0.9901 for the cylinder spacings l/D=2 and 3, respectively.

4.5 Conclusion

The flow velocity and heat transfer in the near field of two identical cylinders in a tandem configuration with spacings of l/D=2 and 3 were obtained using a synchronous PIV-PLIF technique. The heat transfer results were obtained in terms of local, spatially-averaged, and total Nusselt numbers. A higher temperature drop in the gap region between the cylinders was observed for l/D=3 compared to l/D=2 which yielded to a higher heat transfer rate from both cylinders. The increase of heat transfer rate was found to be greater for the downstream cylinder than that for the upstream cylinder. In all studied conditions, it was observed that the value of total Nusselt number increased with an increase in Keulegan-Carpenter number, KC, and frequency parameter, β. In addition, the total Nusselt number for the cylinder spacing l/D=3 was found to be between 7-20 percent higher than that of the cylinder spacing l/D=2 depending on the KC and β.

Table 4.1. Distribution of the instantaneous local Nusselt number at KC=6.42, β=115 and l/D=2 for the left-hand side cylinder.

	Angular location																		
Phase	**θ=0**	**θ=10**	**θ=20**	**θ=30**	**θ=40**	**θ=50**	**θ=60**	**θ=70**	**θ=80**	**θ=90**	**θ=100**	**θ=110**	**θ=120**	**θ=130**	**θ=140**	**θ=150**	**θ=160**	**θ=170**	**θ=180**
ωt=0	4.9	5.25	5.44	5.93	6.3	7.03	7.21	7.39	7.58	7.43	7.05	6.42	5.42	4.49	4.27	4.6	4.81	5.12	5.34
ωt=π/4	4.52	4.72	5.05	5.52	5.91	6.6	6.57	6.55	6.31	6.11	6.2	6.27	6.55	7.22	8.56	9.49	10.24	11.3	11.81
ωt=π/2	4.25	4.32	4.3	4.4	4.56	4.76	5.24	5.83	6.68	8.55	10.5	14.17	17.24	17.7	17.3	16.87	16.52	16.19	15.93
ωt=3π/4	3.61	3.61	3.55	3.47	3.65	4.3	5.44	7.25	9.59	13.32	15.38	15.62	15.21	14.8	14.34	13.93	13.4	13.15	12.77
ωt=π	3.94	3.82	3.61	3.8	3.73	3.81	5.04	6.57	9.52	11.08	11.69	11.1	10.54	9.77	9.22	8.93	8.54	8.38	8.12
ωt=5π/4	6.26	6.67	7.25	7.66	7.47	7.06	6.4	6.29	5.93	5.65	5.44	5.12	5.28	5.32	5.53	5.67	5.74	6.02	6.1
ωt=3π/2	5.83	6.37	7.34	8.49	9.5	10.15	10.08	9.54	9.05	8.26	7.44	6.82	5.67	4.91	4.45	4.56	4.62	4.98	5.47
ωt=7π/4	5.67	6.28	6.71	7.32	8	8.51	9.04	9.36	9.53	9.39	8.68	7.55	6.52	5.2	4.51	4.32	4.27	4.45	4.95
ωt=2π	4.63	5.03	5.65	6.13	6.56	7.27	7.7	8.12	8.31	7.92	7.48	6.66	5.73	5.35	5.24	5.02	5.15	5.46	5.87

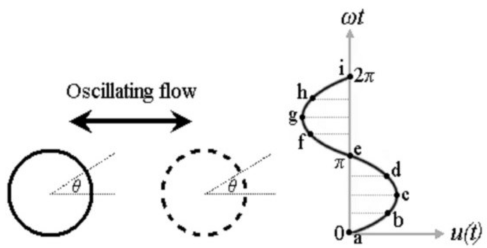

Table 4.2. $Nu \times Pr^{-0.37}$ vs. Keulegan-Carpenter number and frequency parameter for l/D=2.

	***KC*=3.14**	***KC*=6.28**	***KC*=9.42**	***KC*=12.56**	***KC*=15.7**
β=158.1	4.01	5.68	6.59	7.69	8.13
β=248.5	5.10	6.92	8.29	9.62	10.05
β=338.8	6.19	8.18	10.00	11.34	11.71
β=451.7	6.80	9.14	10.96	12.03	12.73

Table 4.3. $Nu \times Pr^{-0.37}$ vs. Keulegan-Carpenter number and frequency parameter for l/D=3.

	***KC*=3.14**	***KC*=6.28**	***KC*=9.42**	***KC*=12.56**	***KC*=15.7**
β=158.1	4.44	6.54	7.79	8.29	9.14
β=248.5	5.51	7.97	9.95	10.43	11.23
β=338.8	6.52	9.41	11.34	12.19	13.10
β=451.7	7.11	10.43	12.62	13.58	14.60

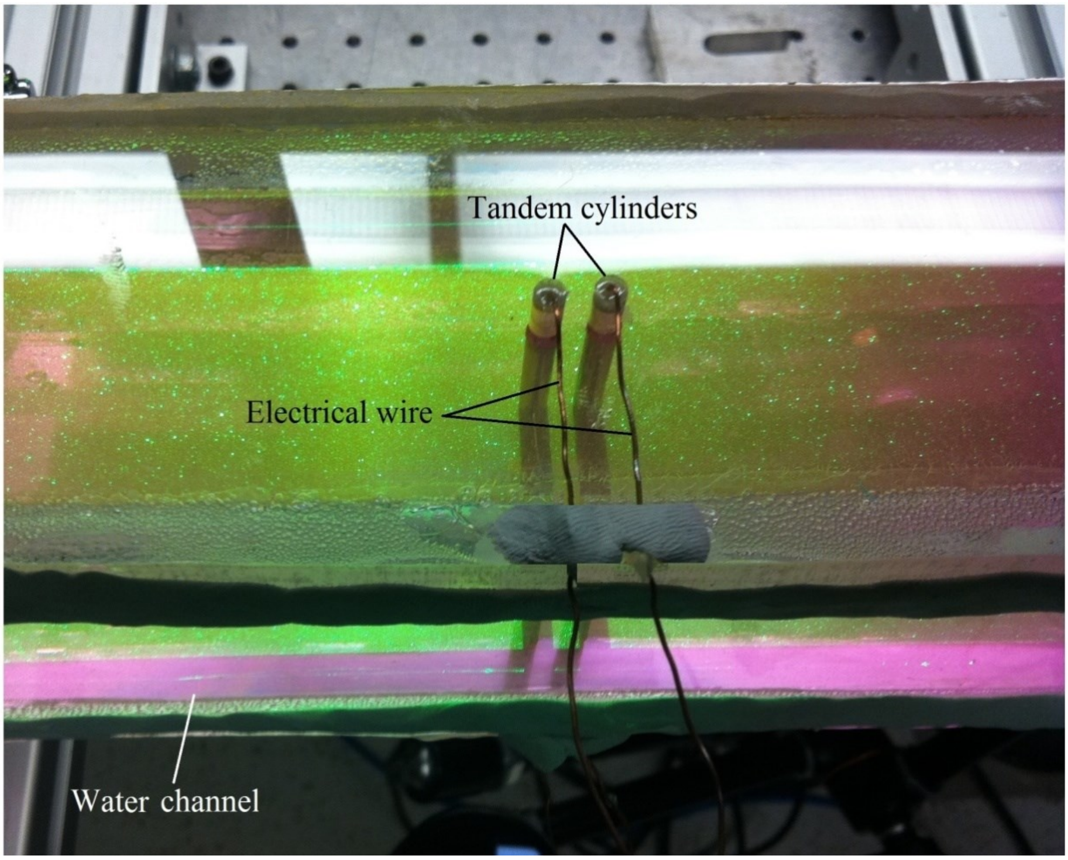

a) l/D=2

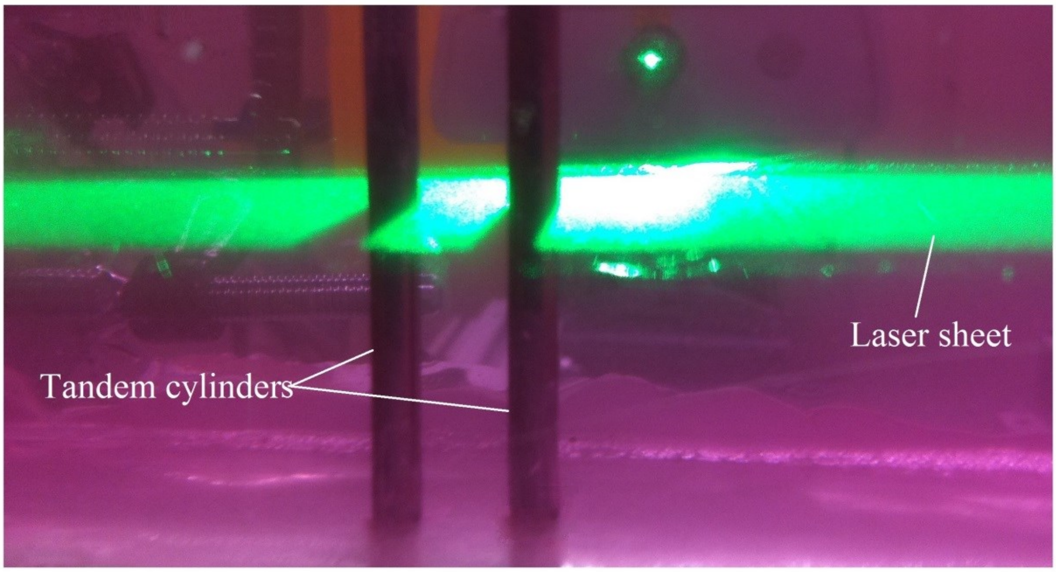

b) l/D=3

Figure. 4.1 Tandem cylinder arrangements.

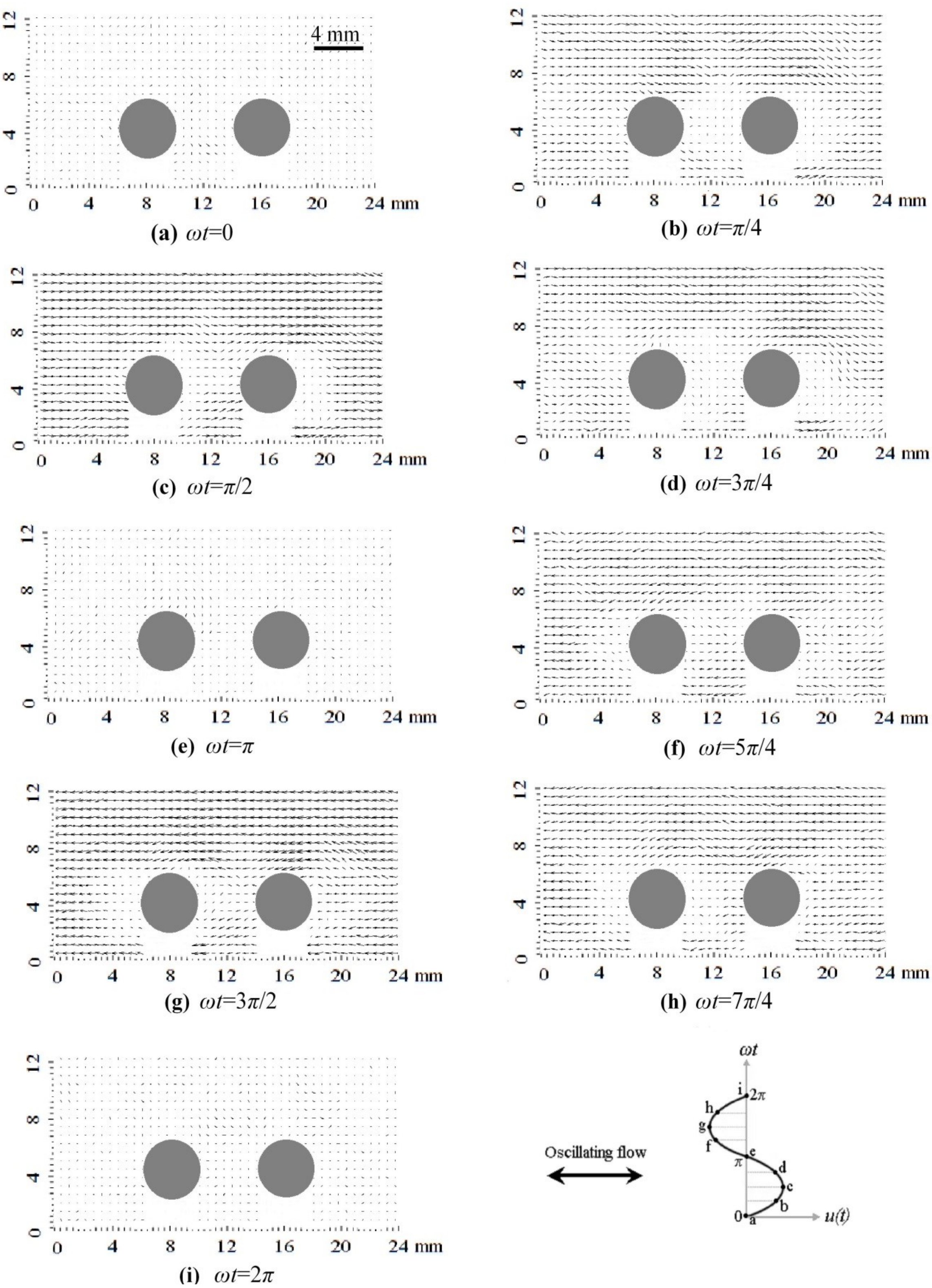

Figure 4.2. Time history of the velocity vector field around the tandem cylinders during one oscillating cycle at KC=3.14, β=158.1 and l/D=2, (a) to (i) correspond to ωt = 0, π/4, π/2, 3π/4, π, 5π/4, 3π/2, 7π/4 and 2π, respectively.

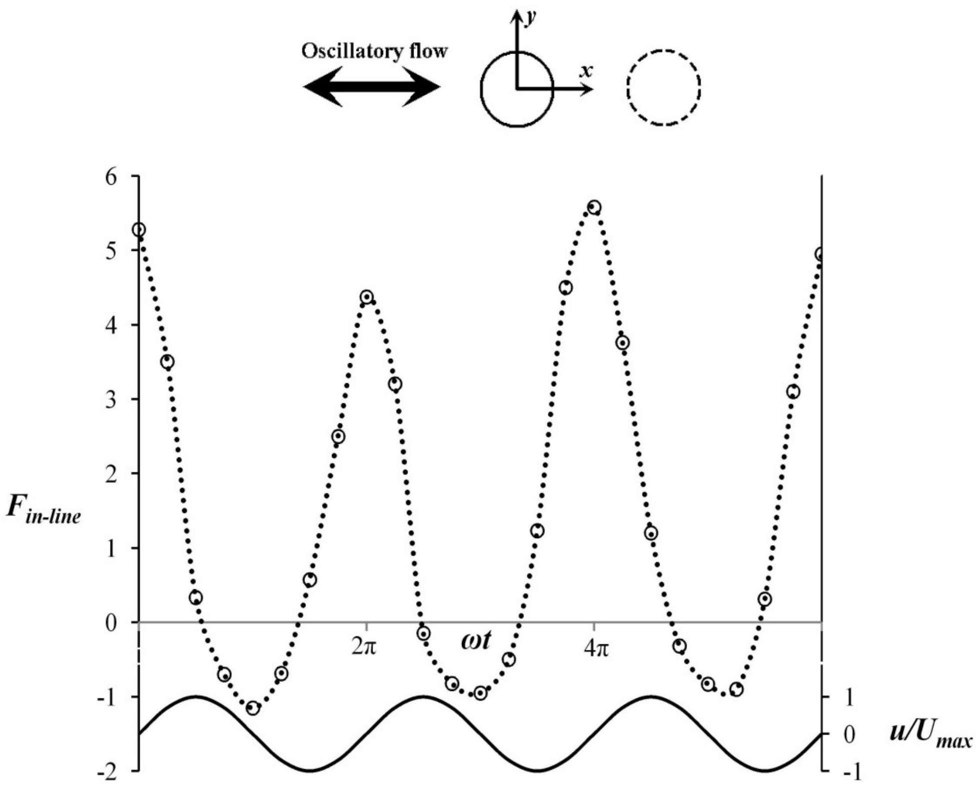

Figure 4.3. Time history of the dimensionless axial force (along x-direction) for the left-hand side cylinder over three periods of oscillation at KC=3.14, β=158.1 and l/D=2, --○--: Dimensionless axial force, ___: Free stream velocity.

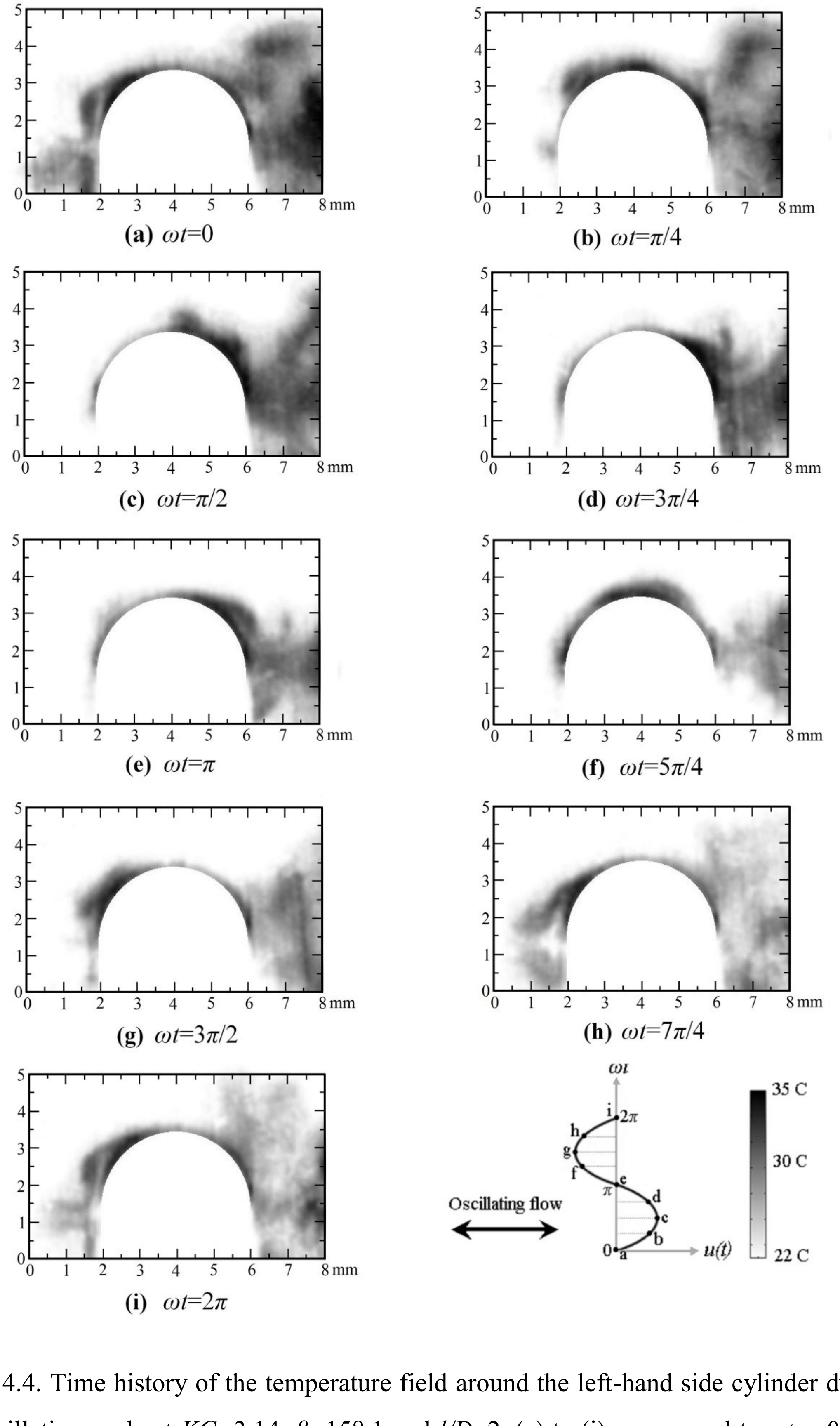

Figure 4.4. Time history of the temperature field around the left-hand side cylinder during one oscillating cycle at *KC*=3.14*,* β=158.1 and *l/D*=2, (a) to (i) correspond to ωt = 0, $\pi/4$, $\pi/2$, $3\pi/4$, π, $5\pi/4$, $3\pi/2$, $7\pi/4$ and 2π*,* respectively.

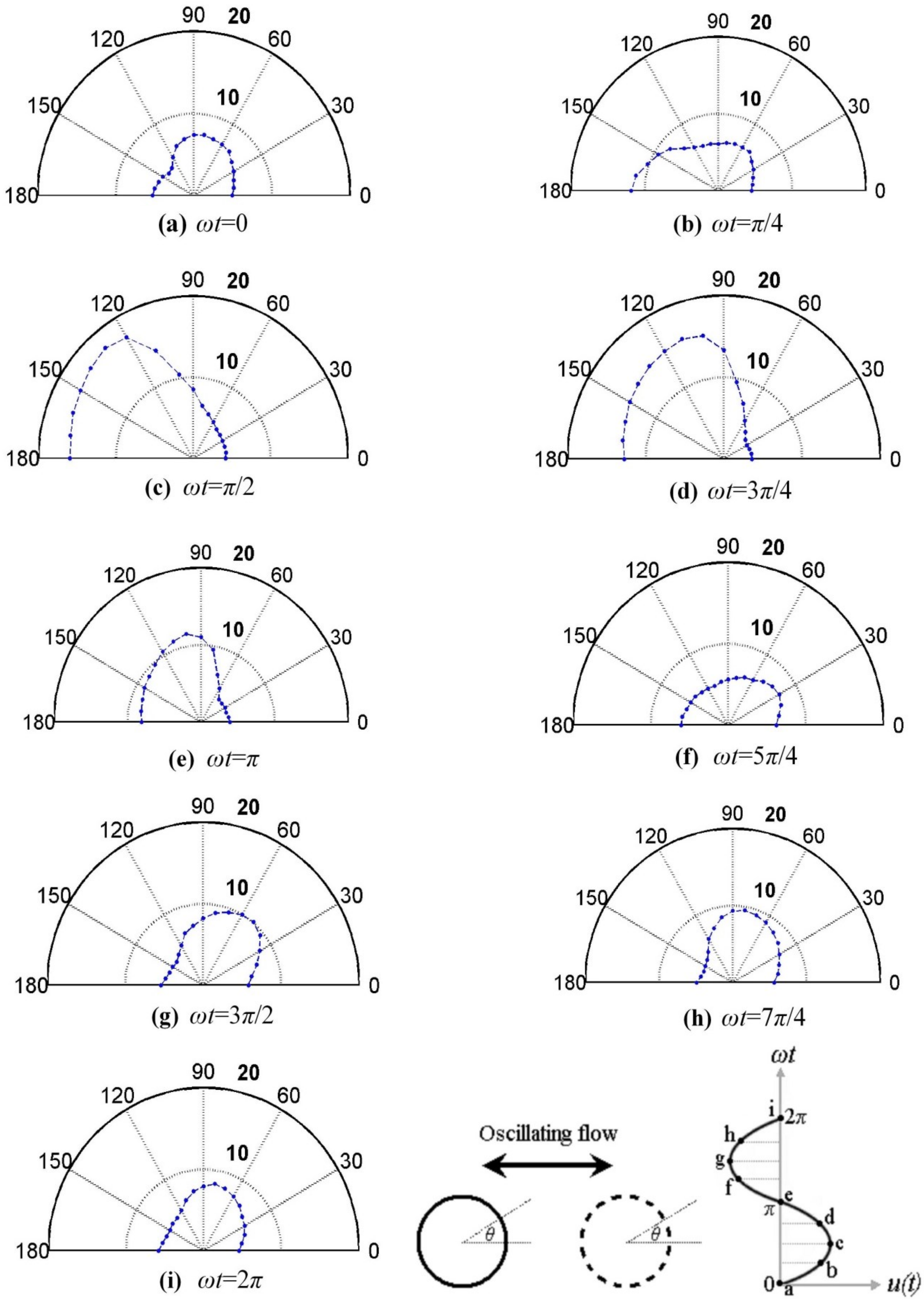

Figure 4.5. Time history of the instantaneous local Nusselt number, Nu_θ, around the left-hand side cylinder at KC=3.14, β=158.1 and l/D=2, (a) to (i) correspond to ωt =0, π/4, π/2, 3π/4, π, 5π/4,3π/2, 7π/4, and 2π, respectively.

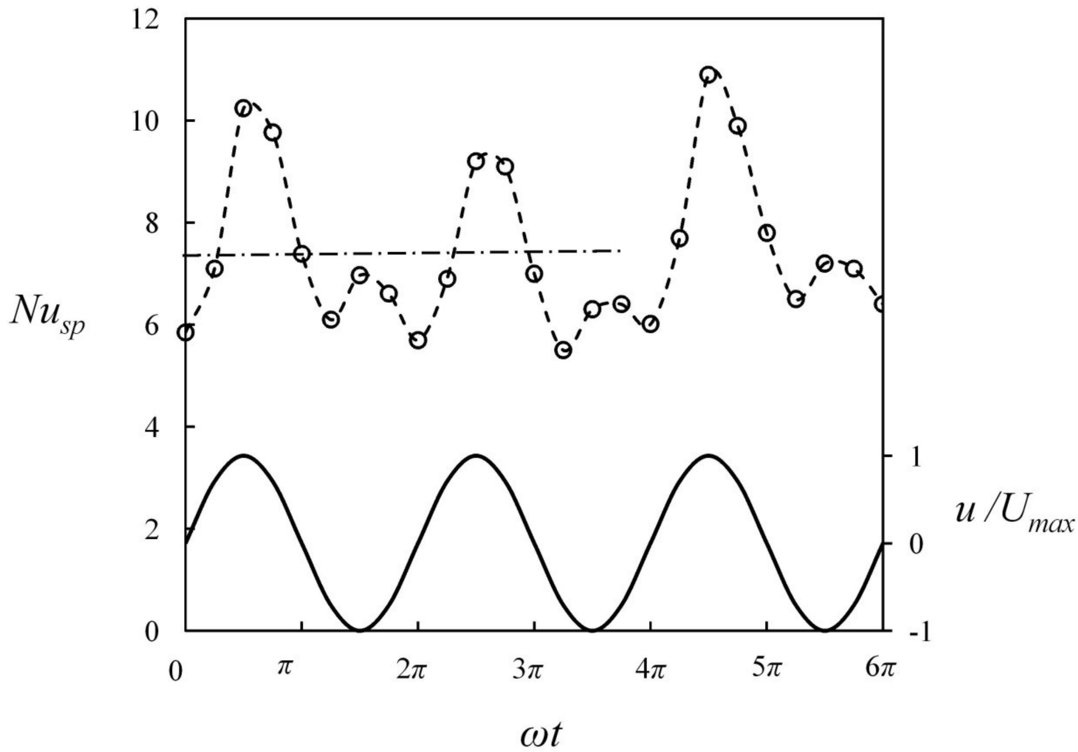

Figure 4.6. Time history of the spatially-averaged Nusselt number during three successive cycles at KC=3.14, β=158.1 and l/D=2, --○--: Spatially-averaged Nusselt number, - • - • -: Total Nusselt number, ──: Free stream velocity.

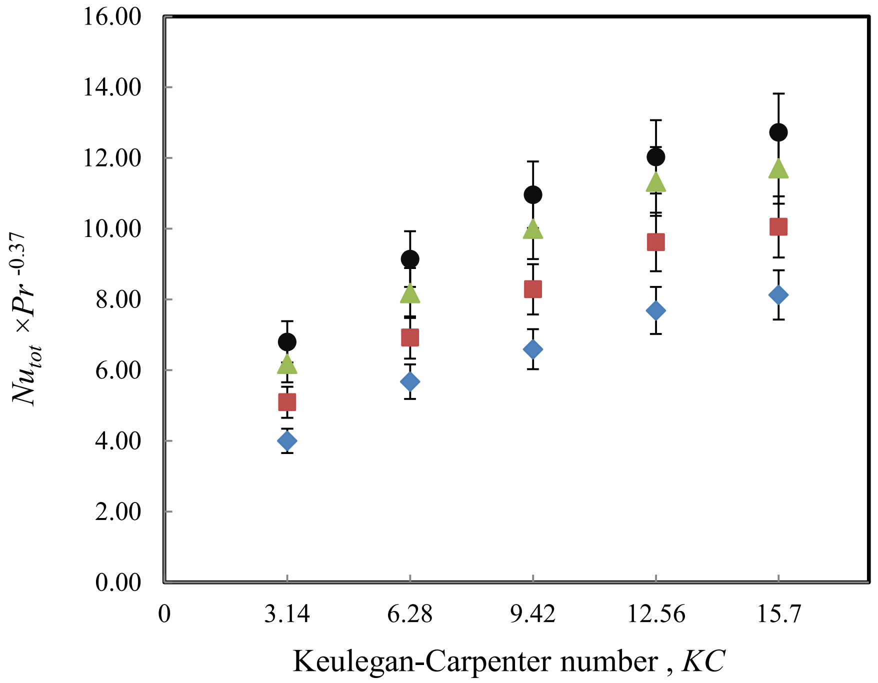

a) l/D=2

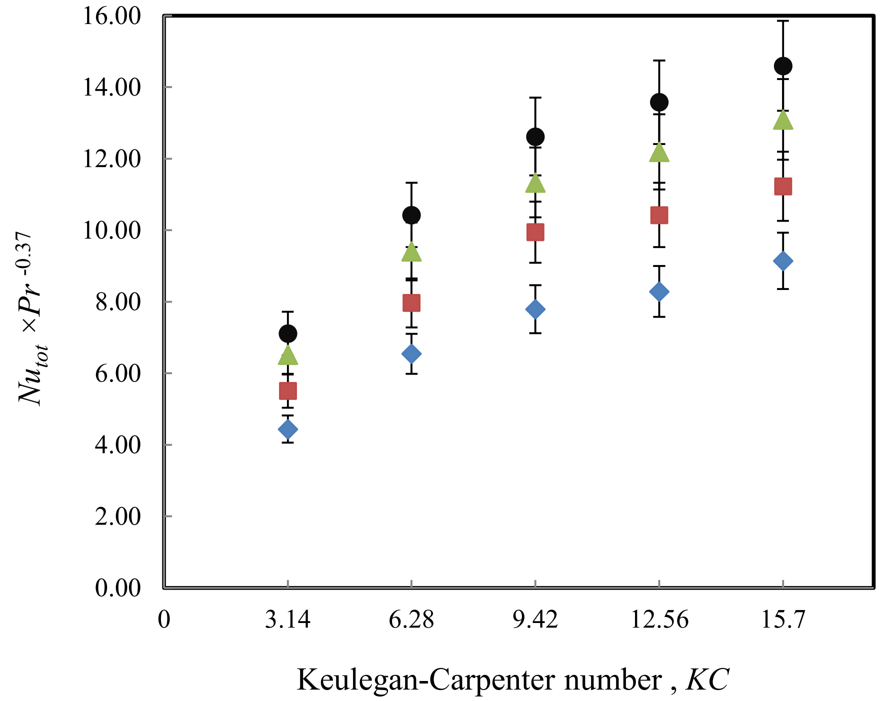

b) l/D=3

Figure 4.7. Total Nusselt number vs. KC and β for l/D=2 and 3, ♦: β=158.1, ■: β=248.5, ▲: β=338.8, ●: β=451.7.

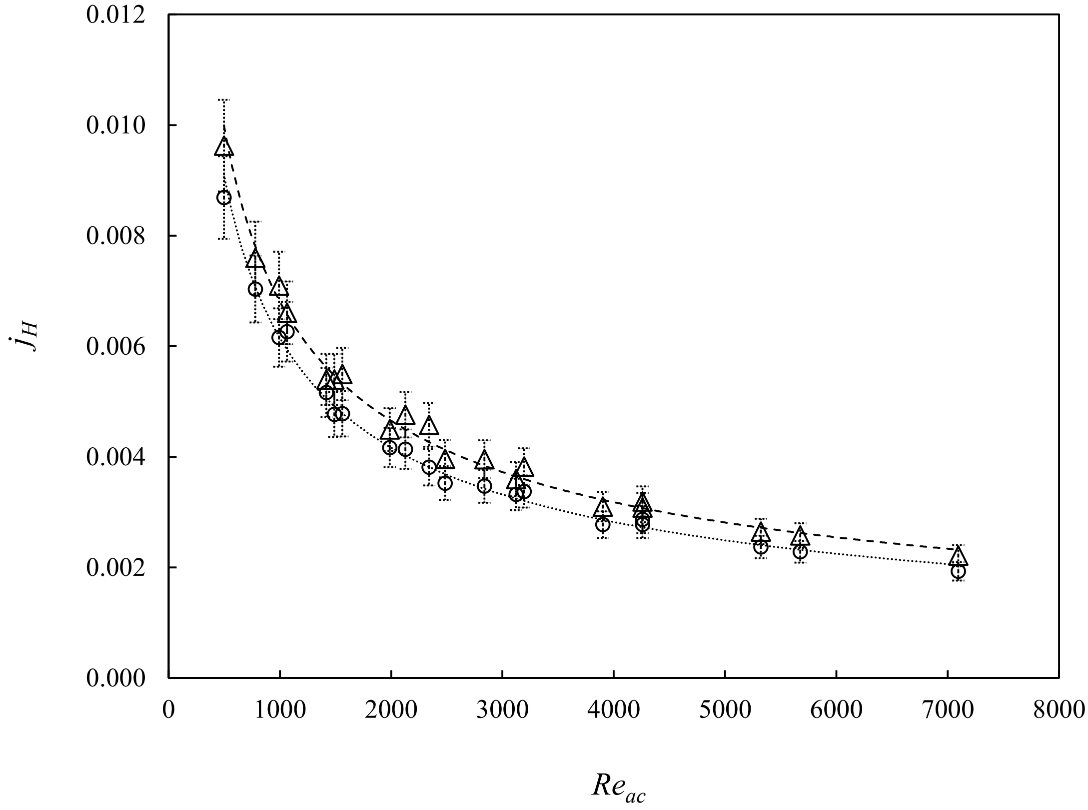

Figure 4.8. Colburn-j factor vs. acoustic Reynolds number.

○: Measured data at *l/D*=2, …..: Regression curve of the measured data at *l/D*=2, Δ: Measured data at *l/D*=3, -----: Regression curve of the measured data at *l/D*=3.

Chapter 5

Heat transfer characterization of an idealized finned tube in oscillating flow

5.1 Introduction

One of the most common methods to enhance the heat transfer rate from a heat exchanger is by attaching fins to the tubes of the heat exchanger. The fins tend to increase the heat transfer surface area and reduce the thermal resistance coefficient which leads to enhanced heat transfer rate from the heat exchangers. Hence, the influence of fins was investigated in the present study in order to evaluate the more realistic heat exchanger configurations. Two longitudinal fins were attached to each side of the cylinder. The flow velocity and the heat transfer in the near field of the finned tube configuration were investigated.

5.2 Description of the experiment

The longitudinal finned tube configuration and its geometrical dimensions are shown in Fig. 5.1. The width of each attached fin was equal to the cylinder radius (2 mm) and their thickness was chosen to be half of their width (1 mm). The longitudinal finned tube was made of copper and was 40 mm long.

The oscillatory flow was generated by an acoustic subwoofer which was connected to a digital signal generator. The frequency of the oscillation flow was chosen within the range of $7 < f < 20$ Hz and the displacement amplitude of the fluid particles was between $D/2 < A_{max} < 5D/2$.

For the flow and thermal field visualization, the synchronized PIV-PLIF technique was utilized as described in details in Chapter 2 of this thesis.

5.3 Flow field visualization

The PIV camera captured the flow field images with a frame rate of 1000 fps. These images were recorded with a resolution of 1280×1024 pixels and each pixel had a pitch of 20 μm. To impose the effect of camera lens magnification factor, a new set of calibration test was obtained.

The velocity vector map of the flow is shown in Fig. 5.2 for different phases during one oscillating cycle at KC=3.14, β=158.1. The study focused on the upper side of the finned tube configuration and the flow field at the lower side was not captured due to the presence of a shadow.

Two recirculation zones were identified at the location of the fin-cylinder attachment, i.e. the base of the fins. These recirculation bubbles were generated due to the compression and expansion of the flow passage and the change in the boundary conditions. Generally, the velocity magnitude of fluid particles inside these recirculation zones was low compared to the free stream velocity. At the phases when the velocity magnitude of the oscillating flow were zero, i.e. ωt=0, π and 2π, the fluid inside the recirculation zones was not yet quiescent, but it was moving under the action of viscous effects. This phenomenon is observable in Figs. 5.2 (a), (e) and (i).

5.4 Temperature field measurements

Post processing of the PLIF images yielded the instantaneous local heat transfer coefficient. The process was fully described in Chapter 2 of this thesis. The PLIF images were captured by a high resolution Photon camera providing a pixel pitch of 20 μm.

5.4.1 PLIF visualization

Fig. 5.3 shows the time variation of the temperature field around the finned tube configuration during one oscillating cycle at KC=3.14 and β=158.1. The temperature field at the upper side of the finned tube configuration was shown in this figure and the thermal field at the lower side was not captured due to the presence of the shadow. The discussed recirculation zones in section 5.3.1, were visible in the thermal field images as well. These zones corresponded to high temperature regions and caused a lower heat transfer rate. The amount of heat transfer rate is quantitatively discussed in the next section.

Thermal field around the finned tube configuration subjected to an oscillatory flow was found to be different from an isolated cylinder under identical conditions. Due to the presence of the attached fins, no stagnation point was found on the surface of the cylinder. In contrast, when the magnitude of the oscillating free stream flow was close to U_{max}, a very thin thermal boundary layer was observed on the head of the fin which was located on the upstream side. This thin boundary layer on the head of the fin led to a high local heat transfer rate. In addition, the thermal field around the finned tube configuration was found to be almost symmetric for the first and second half of the cycle.

5.4.2 Determination of instantaneous local Nusselt number

Fig. 5.4 shows the distribution of the instantaneous local Nusselt number, Nu_θ, on the Developed Semi Circumference (DSC) of the finned tube configuration at KC=3.14 and β=158.1. This figure was sampled at the same phases as those of Fig. 5.2 and Fig. 5.3. The method of calculation of the local Nusselt number was described in section 2.5. The instantaneous local Nusselt number for this case (KC=3.14 and β=158.1) is tabulated in Table 5.1.

Two recirculation zones at the bases of the two fins showed to have the minimum amount of heat transfer. This phenomenon was predictable because those bubbles contained hot attached fluid particles and could not contribute to remove the heat from the finned tube configuration as much as other fluid particles. At the oscillation phases when ωt=3π/4 and 7π/4, the maximum amount of the instantaneous local Nusselt number was observed at around θ=90°. The fin head which was located at the upstream side of the oscillating flow found to have a higher amount of Nusselt number compared to the fin head located at the downstream side. It was concluded that although there was not a stagnation point of high Nusselt number on the cylinder, the fin head could contribute to the removal of the heat to a high extent.

5.4.3 Determination of spatially-averaged Nusselt number

Time history of the spatially-averaged Nusselt number was determined by averaging the local Nusselt number and was shown in Fig. 5.5 during three successive oscillation cycles at KC=3.14 and β=158.1.

The trend of variation of spatially-averaged Nusselt number for the finned tube configuration was found to be similar to that of an isolated single cylinder in Chapter 3. It fluctuated twice the excitation frequency of the oscillating flow and had two maximum extremum and two minimum extremum during one oscillation period. The maximum extremum occurred at the phase ωt=3π/4 and ωt=7π/4 and the minimum extremum happened at the phases ωt=π/4 and 5π/4.

5.4.4 Determination of total Nusselt number

Total Nusselt number was calculated by taking time and space average of the local instantaneous Nusselt number. The calculated values of total Nusselt number for the finned tube configuration is shown in Fig. 5.6 and the corresponding data is tabulated in Table 5.2.

Same as the previous chapters, the value of total Nusselt number increased with an increase in *KC* and β. At higher *KC* values, the effect of β on the total Nusselt number was found to be larger. Higher KC numbers corresponded to the higher displacement amplitudes in which the oscillating flow behaved more similar to a steady flow. That is why the trend of total Nusselt number curved downward for the higher *KC* values. Total Nusselt number of the finned tube configuration was found to be between 23-32 percent higher than that of the tandem cylinders arrangement with the cylinder spacing of l/D=2 under identical *KC* and β values. In addition, it was 11-19 percent more than tandem cylinders arrangement with the cylinder spacing of l/D=3.

5.4.5 Colburn-j factor correlation

Fig. 5.7 shows the variation of the Colburn-j factor with respect to the acoustic Reynolds number for the finned tube configuration. The result as shown in Fig. 5.7 is expressed using the following correlation:

$$j_H = 0.3886 Re_{ac}^{-0.564} \tag{5.1}$$

The R-squared value of the regression curve was 0.9905.

5.5 Conclusion

The flow and heat transfer in the near field of a longitudinal finned tube configuration was investigated in Chapter 5 of this thesis. The flow and thermal fields were visualized utilizing a synchronized PIV-PLIF technique.

Both the flow and thermal fields showed two recirculation zones at the bases of the attached longitudinal fins. These recirculation bubbles contained flow particles with low velocity and high temperature which led to a lower heat transfer rate at these zones. Maximum amount of instantaneous local Nusselt number was observed at around $\theta=90^o$. Spatially-averaged Nusselt number values fluctuated at twice the excitation frequency of the oscillating flow, as for an isolated single cylinder. The total Nusselt number for the finned tube configuration increased with an increase in KC and β and was found to be greater than that for both tandem cylinders arrangements with the cylinder spacing of $l/D=2$ and 3.

Table 5.1. Distribution of the instantaneous local Nusselt number at KC=3.14 and β=158.1 for the finned tube configuration.

	Developed Semi Circumference (DSC) in mm																		
Phase	**0**	**0.5**	**1**	**1.5**	**2**	**2.53**	**3.05**	**3.57**	**4.09**	**4.62**	**5.14**	**5.66**	**6.18**	**6.71**	**7.23**	**7.73**	**8.23**	**8.73**	**9.23**
ωt=0	8.83	8.32	6.86	5.29	3.67	4.01	5.38	6.28	8.77	10.84	13.83	15.26	13.91	12.27	10.9	9.83	9.36	8.65	7.64
ωt=π/4	10.3	9.84	9.42	8.28	7.09	4.64	3.78	3.32	4.29	6.75	9.83	11.26	10.84	10.33	9.8	8.34	7.25	6.14	4.8
ωt=π/2	14	12.54	11.6	10.47	11.5	13.11	14.13	12.52	9.75	6.44	4.14	3.88	4.56	4.98	5.86	6.51	7.49	7.53	8.48
ωt=3π/4	17.4	14.34	11.8	9.75	8.42	8.82	9.78	13.36	17.3	21.29	20.84	17.32	12.3	8.24	6.26	5.33	6.39	7.27	9.19
ωt=π	8.66	8.69	9.27	9.75	11.04	12.53	14.74	15.81	15.27	14.15	11.94	8.08	6.35	4.91	5.37	6.46	8.31	10.27	10.8
ωt=5π/4	6.33	7.08	8.04	8.82	9.74	10.86	11.79	11.29	10.36	7.3	5.24	3.94	4.23	5.27	7.36	8.81	9.9	10.82	11.26
ωt=3π/2	9.75	9.24	8.36	7.38	6.18	5.29	4.39	4.4	4.77	6.31	8.82	11.37	13.19	12.91	11.3	10.83	11.43	12.92	14.71
ωt=7π/4	8.69	7.34	5.72	5.56	7.07	9.02	12.34	17.22	19.27	19.34	15.36	12.29	9.84	8.8	8.84	9.31	10.29	12.91	16.36
ωt=2π	10.6	9.12	7.85	5.37	3.56	3.7	5.64	7.42	10.19	12.33	14	14.32	14.05	13.01	11.82	10.09	9.22	9.14	8.74

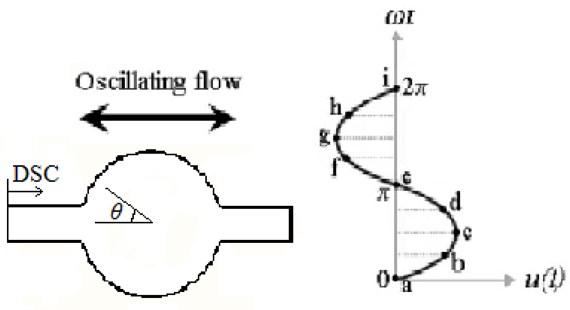

Table 5.2. $Nu \times Pr^{-0.37}$ vs. Keulegan-Carpenter number and frequency parameter for the finned tube configuration.

	***KC*=3.14**	***KC*=6.28**	***KC*=9.42**	***KC*=12.56**	***KC*=15.7**
β=158.1	5.10	7.52	8.59	9.64	10.19
β=248.5	6.58	9.20	10.43	11.89	12.38
β=338.8	7.66	10.80	12.61	14.06	14.87
β=451.7	8.49	11.85	14.68	15.68	16.38

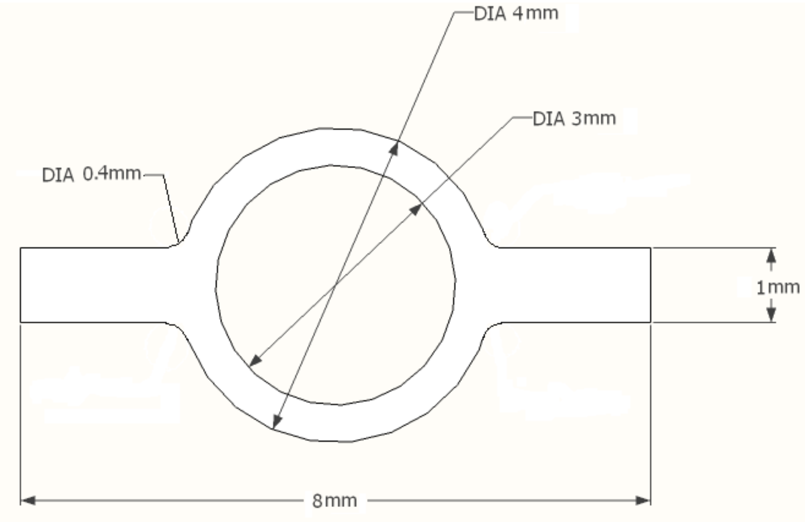

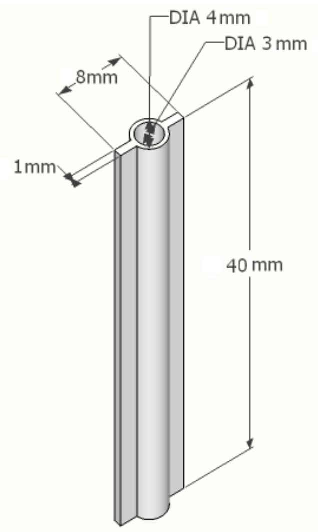

Figure 5.1. Schematic of the longitudinal finned tube configuration.

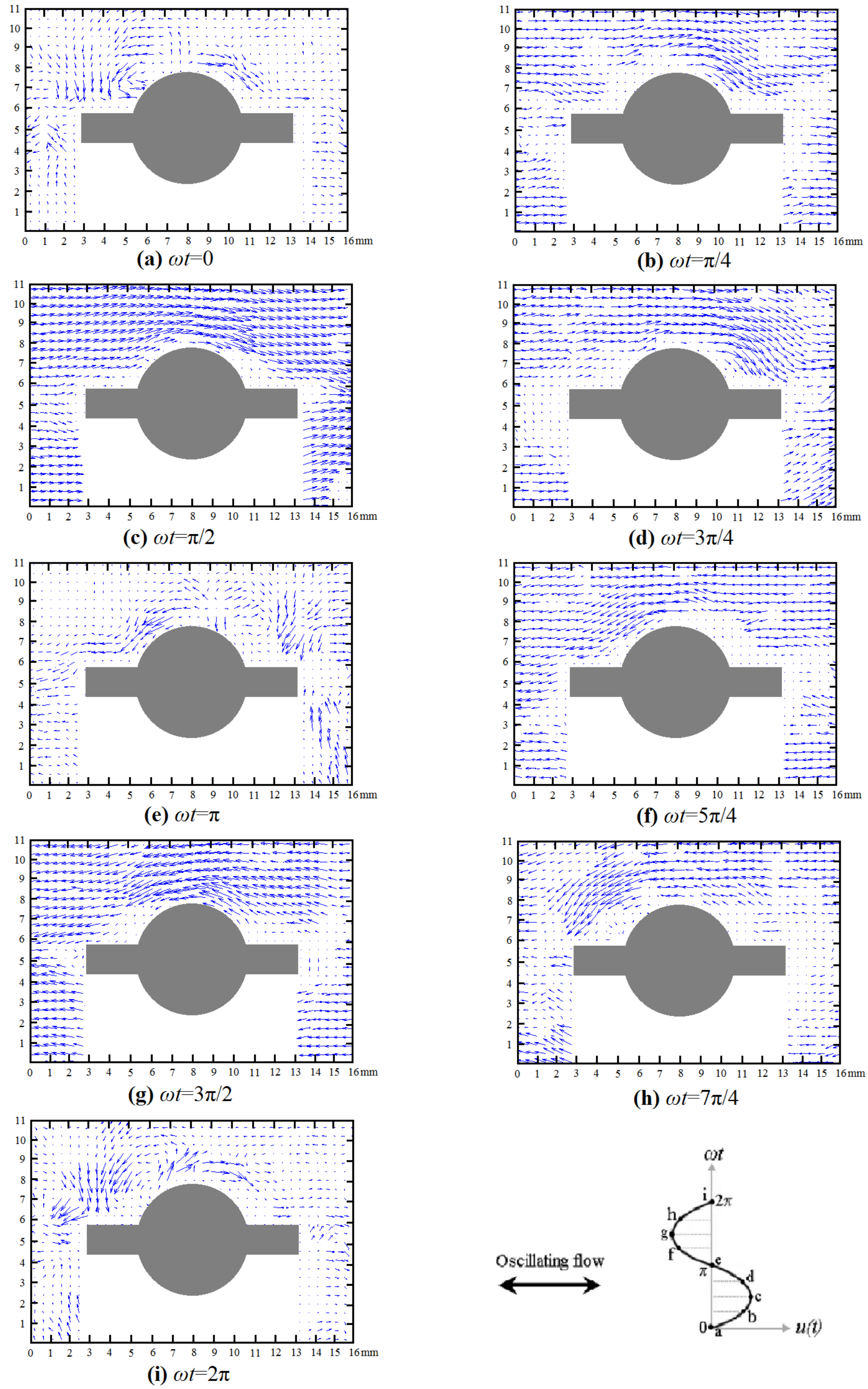

Figure 5.2. Time history of the velocity vector around the finned tube configuration during one oscillating cycle at KC=3.14 and β=158.1, (a) to (i) correspond to ωt = 0, $\pi/4$, $\pi/2$, $3\pi/4$, π, $5\pi/4$, $3\pi/2$, $7\pi/4$ and 2π, respectively.

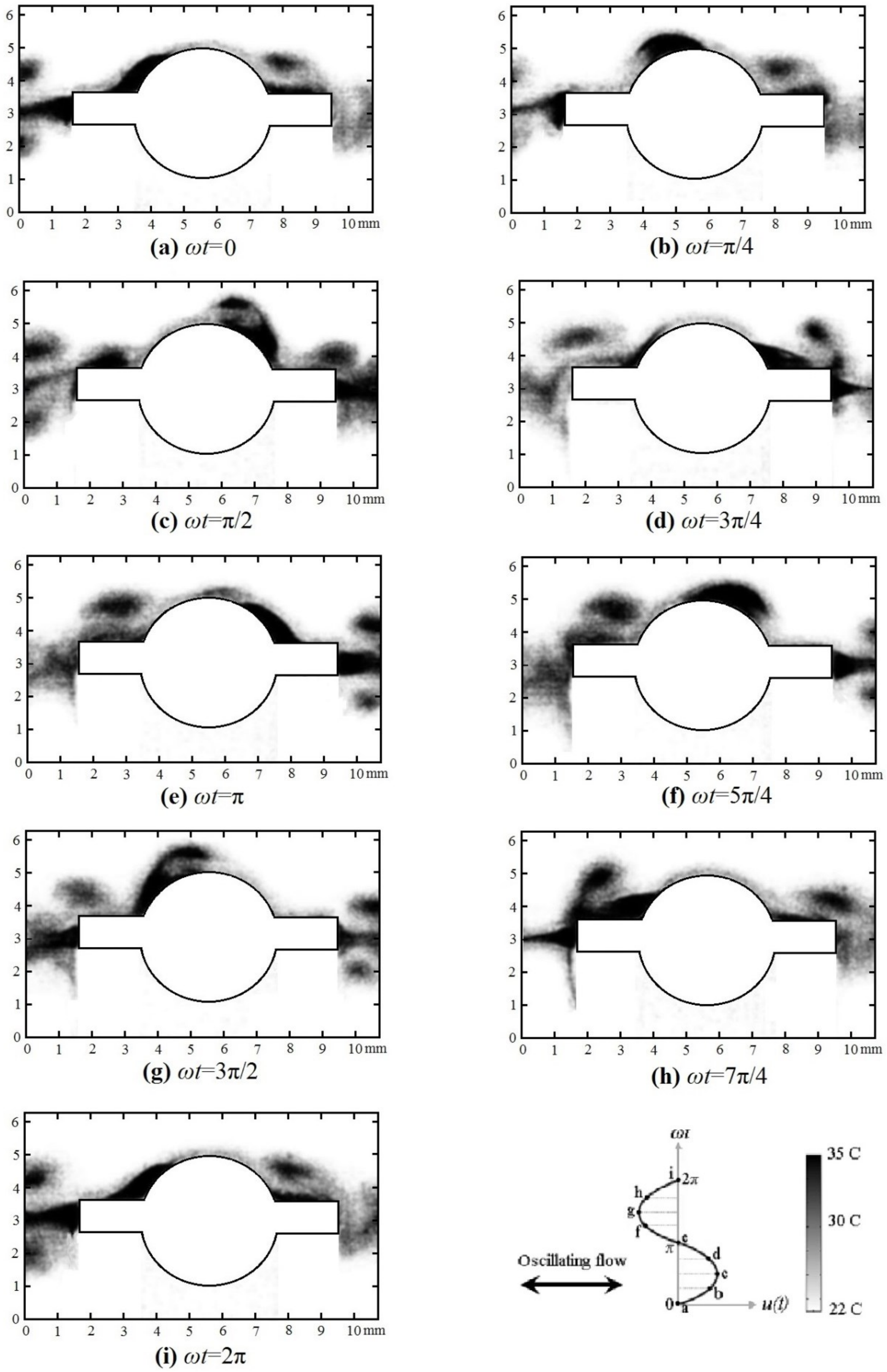

Figure 5.3. Time history of the temperature field around the finned tube configuration during one oscillating cycle at KC=3.14 and β=158.1, (a) to (i) correspond to ωt = 0, $\pi/4$, $\pi/2$, $3\pi/4$, π, $5\pi/4$, $3\pi/2$, $7\pi/4$ and 2π, respectively.

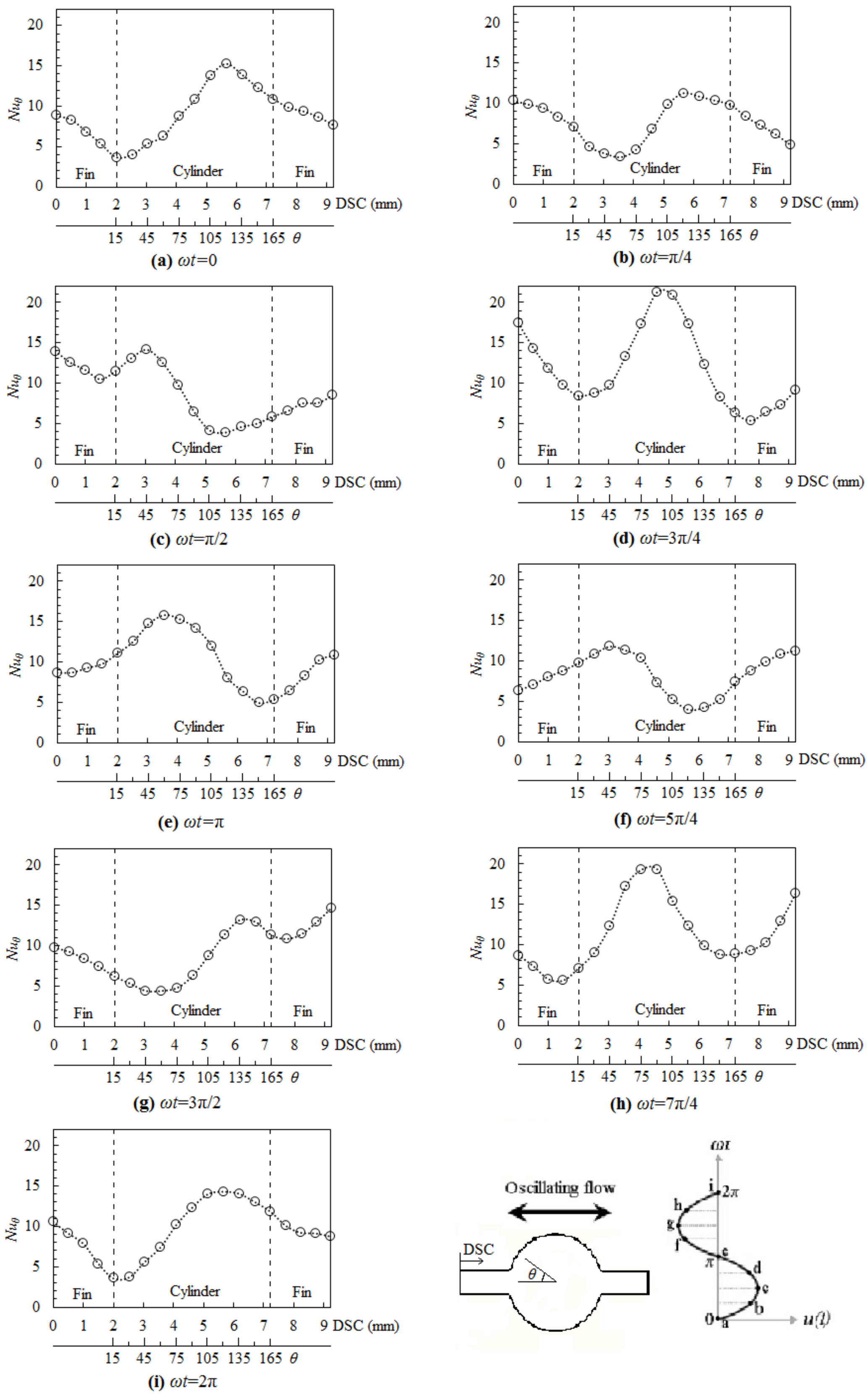

Figure 5.4. Time history of the instantaneous local Nusselt number, Nu_θ, on the Developed Semi Circumference (DSC) of the finned tube configuration at KC=3.14 and β=158.1, (a) to (i) correspond to ωt =0, π/4, π/2, 3π/4, π, 5π/4, 3π/2, 7π/4, and 2π, respectively.

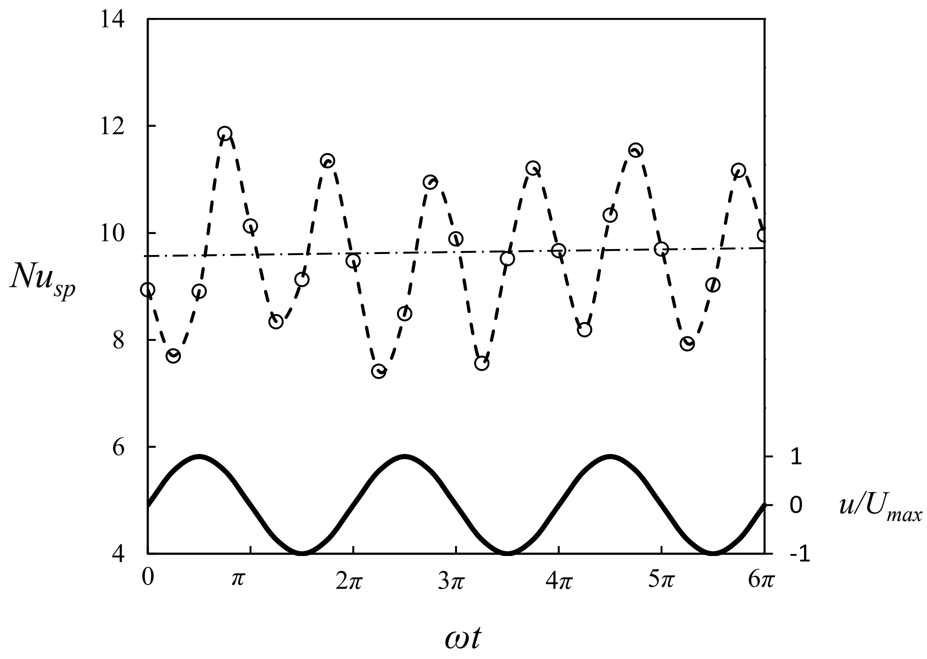

Figure 5.5. Time history of the spatially-averaged Nusselt number during three successive cycles at KC=3.14 and β=158.1, --○--: Spatially-averaged Nusselt number, - • - • -: Total Nusselt number, —: Free stream velocity.

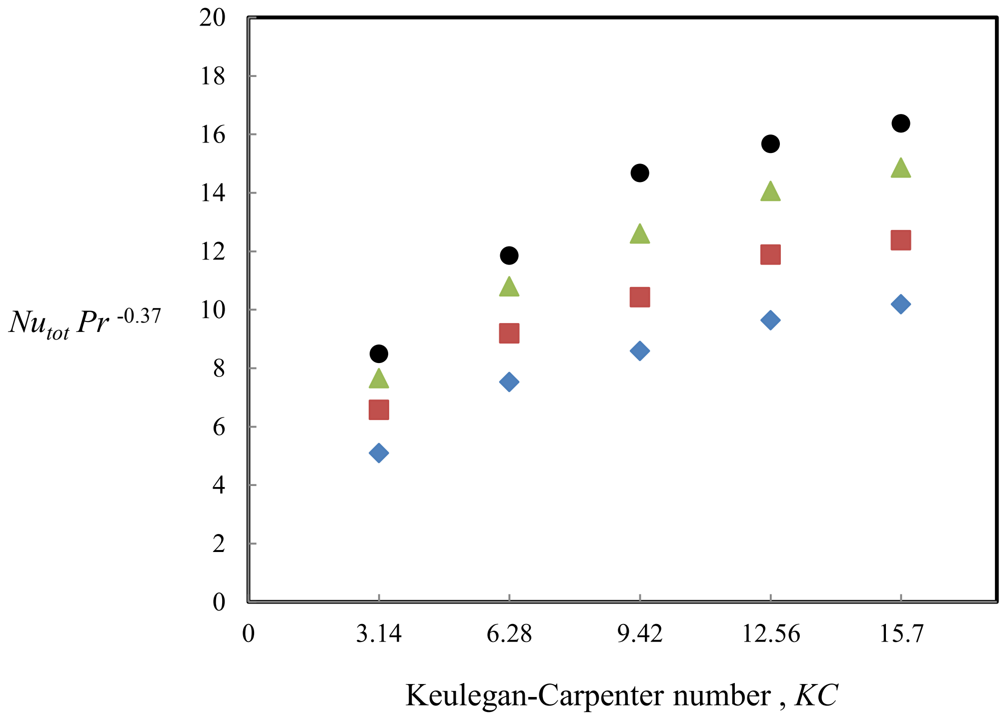

Figure 5.6. Total Nusselt number vs. KC and β for the finned tube configuration,

♦: β=158.1, ■: β=248.5, ▲: β=338.8, ●: β=451.7.

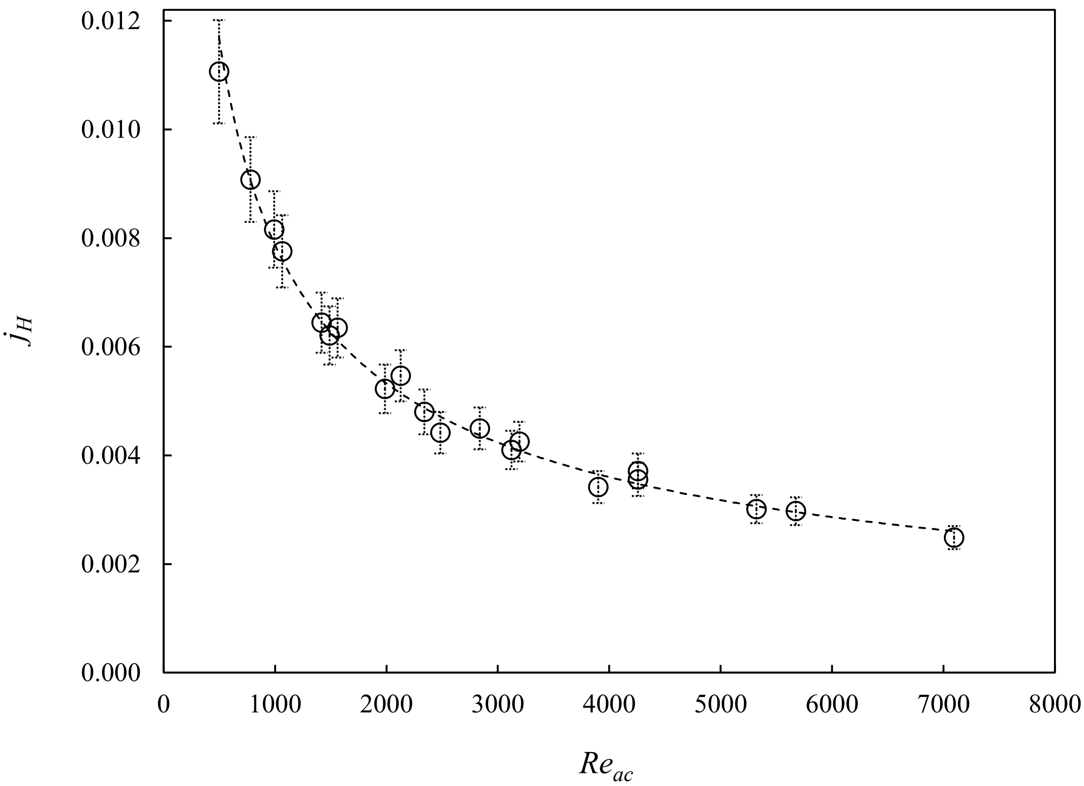

Figure 5.7. Colburn-j factor vs. acoustic Reynolds number for the finned tube configuration. ○: Measured data, …..: Regression curve of the measured data.

Chapter 6

Conclusions and recommendations

Brief concluding remarks and general recommendations for future works are given in this chapter.

6.1 Conclusions

Heat exchangers are an integral part of thermoacoustic cooling devices. Finned tube heat exchangers are the most common heat exchanger types used in thermoacoustic refrigerators. The flow and heat transfer characteristics of heat exchangers immersed in oscillatory flows were found to be different from those in steady state flow. In other words, heat transfer predictions based on steady state correlations are inaccurate for heat exchangers immersed in oscillating flows. This was found to be due to secondary interactions between vortical structures created in any cycle with heat exchanger surface during subsequent cycles. An accurate characterization of heat exchanger in oscillatory flow is necessary for improving the overall performance of a thermoacoustic cooling system. The effect of flow oscillation on heat transfer characteristics related to vortex formation are not fully understood. There is no systematic study available in the literature to investigate the thermal and fluid interactions between oscillatory gas particles and solid structures of heat exchangers in a thermoacoustic system. The present study was the first of its kind to simultaneously visualize the flow and thermal fields and experimentally characterize heat transfer from simplified heat exchanger geometries subjected to oscillatory flows. These geometries included single circular cylinder, tandem cylinders arrangements and finned tube configuration.

The temperature and flow velocity fields in the near field of simplified heat exchanger geometries were experimentally visualized utilizing a synchronized PIV and PLIF technique. High resolution image capturing provided a pixel pitch within the range of 20-38 μm, depending on the test case. Post processing of the visualization images resulted into the determination of local time-dependent, spatially-averaged, and total heat transfer rates as a function of acoustic Reynolds number, Keulegan-Carpenter number and dimensionless frequency parameter.

For the first case, a single circular cylinder was mounted inside a water channel containing the zero-mean velocity oscillating flow. It was found that the vortices shed in the first half of one cycle were convected back near the cylinder during the second half of the cycle. This phenomenon led to creation of warm regions close to the cylinder surface. As a result of this warming effect, the heat transfer from the cylinder was not effectively enhanced by convection as much as for a steady flow. It was also observed that even when the cross-sectional mean velocity was zero or very small, heat could transferred due to the local fluid motion induced by the vortices, shed in one cycle and then convected back by the reversed flow. The spatially-averaged Nusselt number fluctuated at twice the excitation frequency. It was seen that for a given β, when the KC number was increased, both the total Nusselt number and the amplitude of spatially-averaged Nusselt number fluctuation were increased. Data were obtained for cylinders of two different diameters. The results confirmed the reproducibility of the experimental data.

A tandem cylinders arrangement was investigated using similar methods. Two identical cylinders were mounted inside the water channel. The cylinders were in-line with respect to the direction of the free stream flow. Two different center-to-center distance to diameter ratio l/D=2 and 3 were investigated for the tandem cylinders case. It was found that the fluid particles inside the region between two cylinders were blocked due to hydrodynamic interference effects. The axial flow displacement was small compared to the displacement amplitude of the free stream flow. Vortex shedding was not observed from the upstream cylinder for none of the cylinder spacing l/D=2 and 3. The wake was similar to that of a single large bluff body. The thermal field near the upstream cylinder was similar to that of an isolated circular cylinder immersed in an oscillatory flow. A more complex thermal field was observed near the downstream cylinder. It was concluded that the hydrodynamic interference effects were greater for the downstream cylinder compared to the upstream cylinder. A higher temperature drop in the gap region between the cylinders was observed for l/D=3 compared to l/D=2. The displacement of the fluid particle in the gap region was increased when the gap between cylinders was increased, causing a higher local velocity and a lower temperature. The maximum value of the instantaneous local Nusselt number was observed along $110 < \theta < 150$ during the second quarter of the oscillation cycle ($\pi/2 \leq \omega t \leq \pi$), when the flow was decelerating. The variation of the instantaneous local Nusselt number was found to be asymmetrical between the first and second half of a cycle. The upstream cylinder featured higher values of Nusselt number than the downstream cylinder, but both cylinders were found to have a lower Nusselt number than that for an isolated single cylinder under identical conditions. When the cylinder spacing was increased from l/D=2 to l/D=3, a higher value of Nusselt number was detected for both cylinders under a given Re_{ac} number. The hydrodynamic interference was reduced by increasing the gap between the cylinders. The increase of Nusselt number was observed to be larger for the downstream cylinder than for the upstream cylinder. The total Nusselt number for the cylinder spacing l/D=3 was found to be around 8-15 percent higher than that of the cylinder spacing l/D=2 depending on the KC and β values. Fig. 6.1 shows the heat transfer for the different geometries. Compared to an isolated single cylinder, heat transfer rate from tandem cylinders with spacing l/D=2 and 3 were found to be less between 47-64 percent and 27-45 percent, respectively.

In order to enhance the heat transfer from a single cylinder, two longitudinal fins were attached to either side of the cylinder. This modification helped to better mimic the conditions of a real heat exchanger. Two recirculation zones were identified at the bases of either fin. These recirculation bubbles were generated due to the compression and expansion of the flow passage and the change in the boundary conditions. The recirculation bubbles contained flow particles with low velocity and high temperature, which led to a lower heat transfer rate at these zones. It was found that even when the velocity magnitude of the oscillating flow was zero, the fluid inside the recirculation zones was not yet quiescent, but it was moving under the action of viscous effects. Due to the presence of the attached fins, no stagnation point was observed on the surface of the cylinder. In contrast, a very thin thermal boundary layer was observed on the fin head at the upstream side. At the oscillation phases when ωt=3π/4 and 7π/4, maximum amount of instantaneous local Nusselt number was observed at around θ=90°. The value of total Nusselt number increased with an increase in KC and β. At higher KC values, the effect of β on the total Nusselt number was found to be larger. As shown in Fig. 6.1, the heat transfer rate for the finned tube configuration was found to be between 10-29 percent lower than that for an isolated cylinder under identical conditions. It was also found that the heat transfer for the finned tube configuration was larger than both the tandem cylinders arrangements, i.e. between 23-32 percent higher than the case l/D=2 and between 11-19 percent higher than the case of l/D=3.

The present work was the first systematic study to characterize heat transfer from simplified heat exchanger geometries subjected to oscillatory flow. A parametric study was performed for three different geometries and it was concluded that the vortex generation mechanism and heat transfer rates from bluff bodies immersed in oscillatory flows are totally different from those in steady state flows.

6.2 Proposed future work

In a practical standing wave thermoacoustic refrigerator, the heat exchanger is located close to a stack. The presence of the stack at one side of the heat exchanger can change the flow and thermal field and subsequently the total heat transfer rate from the heat exchanger. Therefore, considering the effect of stack on flow and thermal fields is helpful to better characterize the heat transfer from heat exchangers in thermoacoustic applications.

The presented data in this study is based on the experimental measurement and visualization of flow and thermal fields using a combined PIV-PLIF technique. The required facilities are expensive and the experimental procedures require a lot of time and effort. It is recommended that a numerical simulation study be performed based on the presented experimental data. After verification and validation of the simulation, a comprehensive parametric numerical study would help to investigate the effects of geometrical parameters such as width and thickness of the fins, number and orientation of the fins with respect to the free stream flow. Considering different cylinder arrangements such as side-by-side and staggered arrangements is also helpful to extend the knowledge on heat transfer from heat exchangers in oscillatory flows.

DeltaEC [42] is a simulation program which is commonly used to model thermoacoustic devices and can predict how a given thermoacoustic apparatus will perform. The model for the heat exchanger segment used in DeltaEC software is based on the modification of steady state correlations. This modification is not well validated. The experimental data presented in this study can effectively contribute to better analyse and predict the performance of heat exchangers in thermoacoustic applications. Therefore, a separate study is suggested to validate and modify the performance of heat exchanger model in DeltaEC using the presented experimental data. This will be helpful to improve the performance of thermoacoustic systems.

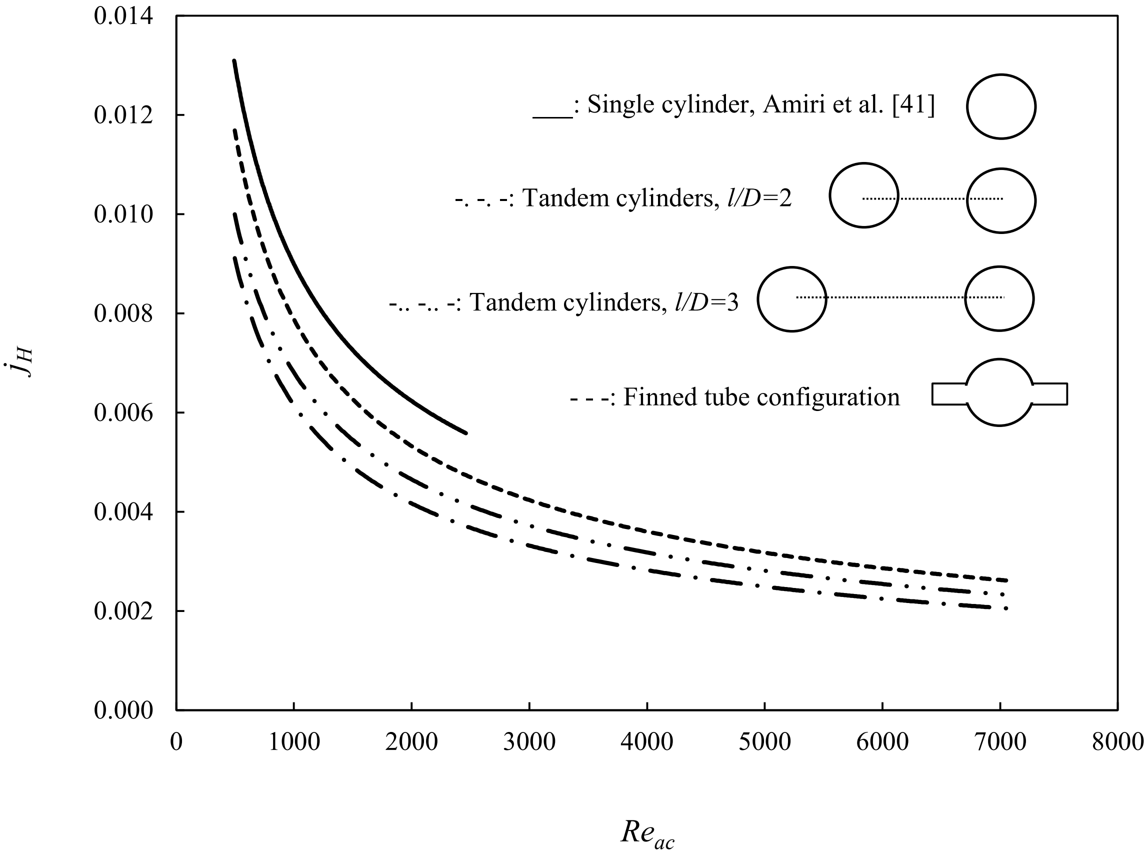

Figure 6.1. Colburn-j factor vs. acoustic Reynolds number for different geometries,

___: Single cylinder, -.-.-: Tandem cylinder with *l/D*=2, -..-..-: Tandem cylinder with *l/D*=3,

- - -: Finned tube configuration.

References

[1] Swift, G.W., Thermoacoustic engines, Journal of the Acoustical Society of America, 1988, 84 (4) 1145–1180.

[2] Wuebbles, D.J., The role of refrigerants in climate change. International Journal of Refrigeration, 1994, 17 (1) 7-17.

[3] Rott, N., Thermoacoustics, Advanced Applied Mechanics, 1980, 20 135–175.

[4] Williamson, C.H.K, Roshko, A., Vortex formation in the wake of an oscillating cylinder, Journal of Fluids and Structures, 1988, 2 355-381.

[5] Obasaju, E.D, Bearman, P.W., Graham, J.M.R., A study of forces, circulation and vortex patterns around a circular cylinder in oscillating flow, Journal of Fluid Mechanics,1988, 196 467-494.

[6] Singhs, S., Forces on bodies in oscillatory flow, PhD thesis, University of London, UK, 1979.

[7] Justesen, P., A numerical study of oscillating flow around a circular cylinder, Journal of Fluid Mechanics, 1991, 222 157-196.

[8] Jeon, D., Gharib, M., On the relationship between the vortex formation process and cylinder wake vortex pattern, Journal of Fluid Mechanics, 2004, 519 161-181.

[9] Barrero-Gil, A., Hydrodynamic In-Line Force Coefficients of Oscillating Bluff Cylinders (Circular and Square) at Low Reynolds Numbers, Journal of Vibration and Acoustics, 2011, 133

[10] Huelsz, G., Lopez-Alquicira, F., Hot-wire anemometry in acoustic waves, Experiments in Fluids, 2001, 30 283-285.

[11] Kang, H.G., Chen, B., Experimental and numerical study of the lift forces on a circular cylinder in sinusoidal flows, Proceedings of the 17th International Conference on Offshore Mechanics and Arctic Engineering, OMAE, Lisbon, Portugal, 5-9 July 1998, Code 49109.

[12] Hann, D.B., Greated, C.A., Particle image velocimetry for the measurement of mean and acoustic particle velocities, Measurement Science and Technology, 1997, 8 656-660.

[13] Hann, D.B., Greated, C.A., The measurement of flow velocity and acoustic particle velocity using particle-image velocimetry, Measurement Science and Technology, 1997, 81517-1522.

[14] Nabavi, M., Siddiqui, M.H.K., Dargahi, J., Simultaneous measurement of acoustic and streaming velocities using synchronized PIV technique. Measurement Science and Technology, 2007, 18 1811-1817.

[15] Mahir, N., Rockwell, D., Vortex formation from a forced system of two cylinders, Part I: Tandem arrangement, Journal of Fluids and Structures, 1996, 10 473-489.

[16] Brika, D., Laneville, A., The flow interaction between a stationary cylinder and a downstream flexible cylinder, Journal of Fluids and Structures, 1999, 13 579-606.

[17] Blanc-Benon, P., Besnoin, E., Knio, O.M., Experimental and computational visualization of the flow in a thermoacoustic stack, Comptes Rendus Mécanique, 2003, 331 17-24.

[18] Mao, X., Marx, D., Jaworski, A.J., PIV measurement of coherent structures and turbulence created by an oscillating flow at the end of a thermoacoustic stack. in: M. Oberlack, et al. (Eds.), Progress in Turbulence II, Springer Proceedings in Physics, 2007, 109 99-102.

[19] Berson, A., Michard, M., Blanc-Benon, P., Measurement of acoustic velocity in the stack of a thermoacoustic refrigerator using particle image velocimetry, Heat Mass Transfer, 2008, 44 1015-1023.

[20] Jaworski, A.J., Mao, X., Yu, Z., Entrance effects in the channels of the parallel plate stack in oscillatory flow conditions, Experimental Thermal and Fluid Science, 2009, 33 495-502.

[21] Leong, K.C., Jin, L.W., An experimental study of heat transfer in oscillating flow through a channel filled with an aluminum foam, International Journal of Heat and Mass Transfer, 2005, 48 243-253.

[22] Mozurkewich, G., Heat transfer from a cylinder in an acoustic standing wave, Journal of the Acoustical Society of America, 1995, 98 2209-2216.

[23] Gopinath, A., Harder, D.R., An experimental study of heat transfer from a cylinder in low-amplitude zero-mean oscillatory flows. International Journal of Heat and Mass Transfer, 2000, 43 (4) 505-520.

[24] Mozurkewich, G., Heat transfer from transverse tubes adjacent to a thermoacoustic stack, Journal of the Acoustical Society of America, 2001, 110 (2) 841-847.

[25] Paek, I., Braun, J.E., Mongeau, L., Characterizing heat transfer coefficients for heat exchangers in standing wave thermoacoustic coolers. Journal of the Acoustical Society of America, 2005, 118 (4) 2271-2280.

[26] Nsofor, E.C., Celik, S., Wang, X., Experimental study on the heat transfer at the heat exchanger of the thermoacoustic refrigerating system, Applied Thermal Engineering, 2007, 27 (14-15) 2435-2442.

[27] Iwai, H., Mambo, T., Yamamoto, N., Suzuki, K., Laminar convective heat transfer from a circular cylinder exposed to a low frequency zero-mean velocity oscillating flow, International Journal of Heat and Mass Transfer, 2004, 47 4659–4672.

[28] Shi, L., Yu, Z., Jaworski, A.J., Application of laser-based instrumentation for measurement of time-resolved temperature and velocity fields in the thermoacoustic system, International Journal of Thermal Sciences, 2010, 49 1688-170.

[29] Cantwell, B., Coles, D., An experimental study of entrainment and transport in the turbulent near wake of a circular cylinder, Journal of Fluid Mechanics, 1983, 136 321-374.

[30] Okajima, A., Matsumoto, T., Kimura, S., Force measurements and flow visualization of bluff bodies in oscillatory flow, J. Wind Eng. Indust. Aerodyn, 1997, 69–71 213–228.

[31] Marchioli, C., Armenio, V., Salvetti, M.V., Soldati, A., Mechanisms for deposition and resuspension of heavy particles in turbulent flow over wavy interfaces, Physics of Fluids, 2006, 18 No. 025102.

[32] Keane, R.D., Adrian, R.J., Optimization of Particle Image Velocimetry, Measurement Science and Technology, 1990, 2 1202-1215.

[33] Arbeloa, T.L., Estevez, M.J.T., Arbeloa, F.L., Aguirresacona I.U., and Arbeloa, I. L., Luminescence properties of rhodamines in water/ethanolmixtures, Journal of Luminescence, 1991, 48-49 400-404.

[34] Coppeta, J., Rogers, C., Dual emission laser induced fluorescence for direct planar scalar behavior Measurements, Experiments in Fluids, 1998, 25 1-15.

[35] Petracci, A., Delfos, R., Westerweel, J., Combined PIV/PLIF measurements in a Rayleigh-Benard convection cell, 13^{th} Int. Symp. on Application of Laser Techniques to Fluid Mechanics, Lisbon, Portugal, 26-29 June 2006, No. 1221.

[36] Coolen, M.C.J., Kieft, R.N., Rindt, C.C.M., Van Steenhoven, A.A., Application of 2-D LIF temperature measurements in water using a Nd : YAG laser, Experiments in Fluids, 1997, 27 420-426.

[37] Moffat, R.J., Describing the uncertainties in experimental results, Experimental Thermal and Fluid Science, 1988, 1 3-17.

[38] Unal, M.F., LIN, J.C., Rockwell, D., Force prediction by PIV imaging: a Momentum-based approach, Journal of Fluids and Structures, 1997, 11 965-971.

[39] Sarpkaya, T., Vortex shedding and resistance in harmonic flow about smooth and rough circular cylinders at high Reynolds numbers, Tech. Rep. NPS-59SL76021, Naval Postgraduate School, Monterey, CA, 1976.

[40] Mahfouz, F.M., Badr, H.M., Mixed convection from a cylinder oscillating vertically in a quiescent fluid, Journal of Heat and Mass Transfer, 2002, 38 477-486.

[41] Amiri, S., Taher, R., Mongeau, L.G., Experimental study of the oscillatory velocity and temperature near a heated circular cylinder in an acoustic standing wave, International Journal of Heat and Mass Transfer, 2014, 69 464-472.

[42] Ward W.C., Clark, J., Swift, G.W., DeltaEC version 6.3b11, Los Alamos National Laboratory. *Available from http://www.lanl.gov/thermoacoustics/DeltaEC.html*